Spring 2013

Three dimensional fluid structural interaction of tissue valves

Vijay Govindarajan
University of Iowa

THREE DIMENSIONAL FLUID STRUCTURAL INTERACTION OF TISSUE VALVES

by

Vijay Govindarajan

An Abstract

Of a thesis submitted in partial fulfillment
of the requirements for the Doctor of
Philosophy degree in Biomedical Engineering
in the Graduate College of
The University of Iowa

May 2013

Thesis Supervisors: Professor Krishnan B. Chandran
Professor H.S. Uday Kumar

ABSTRACT

This thesis presents a stable fluid structural interaction technique to simulate the dynamics of tissue valves including bio-prosthetic heart valves and natural heart valves under physiological Reynolds numbers. A partitioned approach is implemented where the equations governing the flow and the displacement of the structure are solved using two distinct solvers. A FEAP based solid solver is strongly coupled to the p-ELAFINT flow solver using subiteration procedure. The flow solver has been massively parallelized so that the domain can be distributed among several processors. The fixed Cartesian method with adaptive mesh refinement in p-ELAFINT enables us to perform fast and efficient flow computations of problem involving moving boundaries such as heart valve leaflets. To capture the structure deformation, Enhanced Assumed Solid shell element has been implemented into the solid solver which is known for its locking free and superior bending characteristics. Aitken Relaxation method which dynamically computes the relaxation parameter is used for relaxing the solid displacement in the FSI coupling. This helps the subiteration procedure to achieve a faster convergence compared to traditional Subiterative procedures with fixed relaxation parameter. Fung type material model with experimentally derived parameters is used as the constitutive model to capture the realistic solid deformation.

Opening phase of a bicuspid aortic valve (BAV) and a tricuspid aortic valve (TAV) model derived from a patient specific data and a pericardial bioprosthetic valve model were simulated using the FSI algorithm with realistic material parameters under physiological flow conditions. It was observed that all the

bioprosthetic and the BAV models attained its fully open position under 40 milliseconds while the TAV achieved full opening around 45 milliseconds. The bioprosthetic valve and the TAV attained a fully circular orifice while the BAV attained an ellipsoidal shaped orifice at its fully open position. In the BAV, strong vortical patterns were observed at peak systole and recirculation zones were observed near the sino-tubular junction. The work presented in this thesis be seen as a platform from which complex patient specific data can be modeled under physiological conditions and as a base to include contact mechanics with which complete cardiac cycle can be simulated.

Abstract Approved:

_____

Thesis Supervisor

_____

Title and Department

_____

Date

_____

Thesis Supervisor

_____

Title and Department

_____

Date

THREE DIMENSIONAL FLUID STRUCTURAL INTERACTION OF TISSUE VALVES

by

Vijay Govindarajan

A thesis submitted in partial fulfillment
of the requirements for the Doctor of
Philosophy degree in Biomedical Engineering
in the Graduate College of
The University of Iowa

May 2013

Thesis Supervisors: Professor Krishnan B. Chandran
Professor H.S. Uday Kumar

Graduate College
The University of Iowa
Iowa City, Iowa

CERTIFICATE OF APPROVAL

PH.D. THESIS

This is to certify that the Ph.D. thesis of

Vijay Govindarajan

has been approved by the Examining Committee for the thesis requirement for the Doctor of Philosophy degree in Biomedical Engineering at the May 2013 graduation.

Thesis Committee:

Krishnan B. Chandran, Thesis Co Supervisor

H.S. Uday Kumar, Thesis Co Supervisor

Jia Lu

Madhavan L. Raghavan

Nicole M. Grosland

Sarah Vigmostad

To Prema Thulasi and R. Govindarajan, my parents and the foundation of my life.

To Subha Govindarajan, my sister and R. Thejashwini, my wife who have always stood by me.

ACKNOWLEDGEMENTS

I regard myself very fortunate for having advisers like Dr. K.B. Chandran and Dr. H.S. Udaykumar to whom I am indebted for all their advice, support and help thoughout my graduate studies. I also wish to thank Dr. Grosland, Dr. Vigmostad, Dr. M.L. Raghavan and Dr. Jia Lu for all their ideas which have contributed immensely to my thesis. I am also indebted to my family who have continuously supported and stood by me in whatever endeavors I have chosen in my life.

I am also indebted to John Mousel, who played an instrumental role in parallelizing the flow code, for all his help. I also recognize the contributions of past graduate students in my lab, Sreedevi Krishnan, Sai Marella and Sarah Vigmostad and my lab mate, Paul Jermihov for all their contributions.

I thank the past and the present BME administrative staff, Lorena Lovetinsky, Angela Dickey, April Erickson, and Courtney Bork for all their support. I am also grateful to the Department of Biomedical Engineering and the University of Iowa as a whole for the rich educational experience and everything else they have given me.

TABLE OF CONTENTS

LIST OF FIGURES……vi

CHAPTER

I. INTRODUCTION AND BACKGROUND…… 1

1.1 Brief anatomy, pathology of heart valves and treatment modalities…… 2
1.1.1 Aortic valve…… 3
1.1.2 Mitral valve…… 5
1.2 Bioprosthetic valves…… 7
1.2.1 Computational studies on tissue heart valves…… 9
1.3 Specific aims…… 14

II. METHOD…… 16

2.1 Flow solver…… 17
2.2 Modeling Blood as a Newtonian Fluid…… 24
2.3 Solid solver with Enhanced Assumed Strain Solid Shell Element.. 24
2.4 Enhanced Assumed Strain Solid Shell element…… 25
2.4.1 Constitutive model…… 31
2.4.2 Element test…… 32
2.4.3 Coupling…… 34
2.5 Validation of FSI Algorithm…… 38

III. FLUID STRUCTURAL INTERACTION OF PERICARDIAL BIOPROSTHETIC VALVE…… 44

3.1 Results…… 46
3.2 Discussion…… 50

IV. FLUID STRUCTURAL INTERACTION OF BICUSPID AORTIC VALVE…… 55

4.1 Valve Geometry and simulation conditions…… 58
4.2 Results…… 61
4.3 Discussion…… 66

V. FLUID STRUCTURAL INTERACTION OF NORMAL (TRI-LEAFLET) AORTIC VALVE…… 69

5.1 Results…… 71

VI. SUMMARY, LIMITATIONS AND FUTURE STUDIES..... 76

6.1 Validation..... 78
6.2 Limitations..... 79

REFERENCES..... 82

LIST OF FIGURES

Figure

1. Implementation of the ANS method…… 28

2. Mesh of Cantilever beam cases for testing mesh insensitivity…… 33

3. Comparison of deformation from the skewed and uniform mesh that shows the solution is insensitive to mesh distortion…… 34

4. Flow chart of the strongly coupled FSI Algorithm…… 36

5. Velocity contours at various stages of simulation of the flexible flap in a converging channel used for validation of the FSI Algorithm…… 40

6. Local mesh refinement updates the mesh based on flow gradients without any user intervention …… 40

7. Stages of displacement color coded by time. Figure on the right panel shows the tip displacement as a function for time…… 41

8. Results of flap displacement versus time obtained by Idelsohn et al. [60] for comparison with the present study…… 42

9. Subiterations are performed with in a time step in order to deal with the instability due to the tightly coupled system…… 43

10. Details of the pericardial bio prosthetic valve simulation (a) Shows a photograph of a typical bioprosthetic valve. (b) Geometry and boundary conditions used in this study. Dimensions are obtained from an FSI study conducted by de Hart et al. (c) shows the leaflet from the aortic view with regions of interest marked …… 45

11. Initial configuration of the valve (a) leaflets are in fully closed position. (b) Interfacial pressure contours in Pascal at 0.017 sec. (c) Local mesh refinement refines mesh at regions of high flow gradient… 46

12. Axial velocity contour and von mises stress distribution during the various stages of valve opening. The curvature of the leaflets change during the opening phase and valve attains a fully open position around

35 millisecond which is similar to physiological situation (a) 0.0125 s (b) 0.031 sec (c) 0.045 sec..... 49

13. Subiterations are performed to deal with the instantaneous response of the leaflets to fluid force (a) Shows the subiteration number versus time step for the present study. (b) Shows the number of grid cells used for computation versus time..... 51

14. Axial velocity profile of the bioprosthetic valve at final stages of opening. (a) 0.031 sec (b) 0.045 sec..... 53

15. Comparison of present result with previous bioprosthetic valve studies: (a and b) shows the 3d valve deformation at various stages of valve opening and slices extracted at mid plane of the leaflet geometry. (c) Valve deformation obtained from 3D flow loop experiments. (d) 3D FEM computation (e) 2D FSI study..... 54

16. The bicuspid aortic valve geometry with dimensions. (a) View from the aortic side. LCS, RCS and NCS are left, right and non-coronary sinuses respectively. (b) Shows the computational domain with the leaflet and the aortic sinuses and the applied boundary conditions. Simulation is continued until 100 milliseconds. All dimensions are in cms..... 60

17. First two panels shows the axial velocity contours and the third panel shows the von mises stress distribution at various stages of valve opening. Flow results show that the developed jet is off centered and near the commissural region and the deformation of the valve also appears to be asymmetrical resulting in an ellipsoidal shaped orifice..... 63

18. The axial velocity contours and the Vorticity contours at time (a) 0.050 sec (b) 0.075 seconds (c) shows the corresponding axial velocity profiles. The axial velocity contours and the vorticity contours during peak systole shows strong jet development, vortical structures and recirculation zones near the sino-tubular junction..... 64

19. A high density mesh was used to capture the flow at a physiological Reynolds number. Use of LMR enabled efficient computing. The simulation started with 3 million grid cells and as the increased with the flow and finally reached 10 million grid points which enabled adequate flow resolution. (a) The number of cells recruited for the computation (b) subiteration versus time. (c) Shows the Cartesian mesh with LMR in action..... 67

20. The normal aortic (tri-leaflet) aortic valve geometry. (a) Shows the computational domain with the leaflet and the aortic sinuses and the applied boundary conditions. (b) View from the aortic side. LC, RC and NC are left, right and noncoronary leaflets respectively..... 71

21. The axial velocity contour and root mean square of displacement at initial stages of valve opening (a) 1.25e-04 s (b) 0.0125 sec (c) 0.025 sec (d) 0.0415 sec..... 73

22. The axial velocity contour and root mean square of displacement at final stages of valve opening (a) 0.051 s (b) 0.06 sec (c) 0.068 sec (d) 0.078 sec.... 74

23. The axial velocity profile of a normal aortic (tri-leaflet) aortic valve during peak systole. The velocity was measured at the sinutubular plane as marked in yellow. Axial velocity profile shows a skewed pattern with a mean velocity around 1.5 m/sec..... 75

CHAPTER I
INTRODUCTION AND BACKGROUND

Heart valves can fail due to various reasons such as rheumatic fever, degenerative calcification (hardening of the valve), mitral valve prolapse (results in regurgitation of the blood) or as a result of inherent failure from congenital heart disease (an estimated 36,000 infants are born each year with congenital heart disease). More than 250,000 heart valve implantations are performed each year in hope of treating the patients with above conditions and enabling them to lead a healthier life. There are two major types of heart valves available for implantation today: mechanical and tissue valves. While the mechanical heart valves have a great durability and generally lasts a life time, problems associated with implanted valves include thromboembolic complications, anticoagulant-related hemorrhage, tissue overgrowth, infection, paravalvular leak and valve failure owing to material fatigue or chemical change [1,2,3] once implanted. On the other hand, the tissue valve has an advantage of presenting a flow dynamics that is close to the natural heart valves; hence patients implanted with tissue valve need not be concerned about thromboembolism. But the shortcoming of tissue valve is its limited life after implantation which calls for replacement involving repeated surgeries and associated complications. A comparative study between the outcomes of the patient who received mechanical valve and bioprosthetic valve observed that the rates of survival and freedom from all valve related complications in patients were similar for both type of valves. However the study noted that bleeding complications were frequent among those who were implanted with mechanical valves and bioprosthetic valves encountered structural failure [4]. With time tissue valve

deteriorate due to calcification that stiffens the valve. This leads to valve malfunction and thus affecting the pumping efficiency of the heart. Hence for younger patients, mechanical valves are preferred and tissue valves are preferred for older patients. Efforts are being made to understand more about tissue valve and polymeric valve failure with a goal to improve its durability so that, if achieved can be implanted for younger patients as well [5, 6]. It has been hypothesized that bio-prosthetic valve deterioration is due to the hemodynamic forces intrinsic to the tissue. Studies have shown that the clinical failure of bio-prosthetic valve occurs mainly because of the material deterioration and associated calcium deposits at highly stressed regions such as the valvular commissures and the regions of maximal flexion [7].

1.1 Brief anatomy, pathology of heart valves and treatment modalities

Heart valves ensure unidirectional blood flow through its chambers. The tricuspid valve ensures forward flow between the right atria and the ventricle. The pulmonic valve regulates blood flow between the right ventricle and the pulmonic veins when blood is being pumped to the lungs for oxygen enrichment. Oxygenated blood arrives at the left heart and is pumped into the systemic circulation by the left ventricle through the aorta. The mitral valve regulates the flow between the left atrium and the left ventricle and the aortic valve ensures forward flow from the left ventricle into the aorta. During the ventricular filling phase (diastole), the aortic and the pulmonic valves are in closed position. At this time the mitral valve and the tricuspid valve open to allow filling. The aortic and the pulmonic valves open during the systolic phase when the ventricles are contracting and allow blood to be

pumped into the systemic and pulmonic circulation. To prevent backward flow in the atria, the mitral and the tricuspid valves close during systole. The tricuspid and the pulmonic valves of the heart withstand about 30 mmHg and 15 mm Hg blood pressure during closure respectively whereas the valves on the left side, namely aortic and the mitral valve withstand about 80 mmHg and 120 mmHg respectively and hence are subjected to a harsher environment. It is also worthwhile to note that the valves on the left side of the heart are more susceptible to diseases and hence make this an interesting area of research [8].

1.1.1 Aortic Valve

The Aortic valve is made up of three cusps (or leaflets) which are attached to a fibrous ring which are embedded in the fibers of ventricular septum and the anterior leaflet of the mitral valve. It is anisotropic, inhomogeneous and viscoelastic like most of the biological tissues. The aortic leaflet consists of three distinctive layers called the fibrosa on the aortic side with dense fibrous layer in the belly of the leaflet, spongiosa, the middle layer made up of loose connective tissues, proteins , and glycosaminoglycans (GAGs) and finally, the layer covering the ventricular side is called ventricularis which is made up of both elastin and collagen. Ventricularis is thin compared to fibrosa and its smooth surface aids in the flow of blood offering little resistance. The length of the leaflet of an aortic valve is greater than the annular radius and hence, when the valve closes, overlapping of leaflet tissue occurs from each leaflet which forms a coaptation surface called the lunula. This coaptation phenomenon ensures that the valve is perfectly sealed at the end of the decelerating phase of the cardiac cycle where the blood is being pushed back [8].

Diseases affecting the heart valve either obstruct the forward flow (stenosis) or flow leakage across fully closed valve (regurgitation) resulting in an incompetent valve. The stenosis of the aortic valve causes varying degrees of left ventricular outflow obstruction thus affecting the overall pumping efficiency of the heart. The stenosis can either be congenital (in BAV) or acquired. Congenital malformation of the leaflet is often associated with development of progressive fibrosis and calcification which further leads to the narrowing of the valve. BAVs are also associated with other complications such as infective endocarditis, aortic dissection and dilation of ascending aorta. On the other hand, patients over age of 70 typically have senile aortic stenosis. In these cases, leaflets start out as normal valves maintaining its normal functionality, but with age, valve sites develop calcification and thickening resulting in a stenosed (stiffer leaflets) valve. The standard treatment for aortic valve stenosis is valve replacement where the type of the replacement valve is determined according to patient conditions. Although balloon aortic valvotomy reduces transvalvular pressure gradient and provides clinical improvement, this is not seen as a long term cure as restenosis has been observed to occur within six months thus making this procedure an undesirable substitute to valve replacement [9].

Aortic regurgitation results from the structural defect of aortic valve which disables the valve from an effective closure thus allowing backward flow into the left ventricle. The causes of this disease can vary from infective endocarditis, aortic dissection, rheumatic fever, BAV, Marfan syndrome etc. Treatment modalities for aortic regurgitation are the following [9].

- Aortic homograft: Patients aorta is replaced with a donor's aorta.
- Pulmonary autograft (Ross procedure): Patients pulmonary valve replaces the diseased aortic valve.
- Valve replacement: Patient is implanted with a bio-prosthetic valve or a mechanical heart valve.
- Aortic valve repair: Surgical repair of the aortic valve so that patients own valve can be retained.

1.1.2 Mitral Valve

The mitral valve is a bicuspid valve that is primarily composed of the anterior and posterior leaflets, the valve annulus where the leaflets are attached, the chordae tendinae and the papillary muscles. The optimum performance of the mitral valve relies upon the intricate interactions between all of the above. The mitral annulus is attached to the atrial and the ventricular walls and the aortic root, which forms the base of the valve leaflets. The annulus is composed of a dense collagenous tissue surrounded by muscles. During the different phases of the cardiac cycle, the mitral valve goes through a series of changes not only in size but also in its orientation. The annulus is known to have a three dimensional saddle-shaped form and its circumference ranges from 8-12 cm during diastole. The leaflets of the mitral valve are actually one continuous piece of tissue with commissures which separate the tissue into anterior and posterior leaflets. A mitral valve tissue primarily contains collagen-reinforced endothelium and also with striated muscle cells, nerve fibers and blood vessels. The anterior leaflet is comparatively larger than the posterior leaflet and has a roughly semi-lunar shape whereas the posterior

leaflet assumes a quadrangular shape. The combined surface area of the leaflets is approximately twice the orifice area, allowing a large leaflet coaptation during closure. The chordae tendinae are attached to the free edges of the leaflets in a fan like distribution at the commissures. On the other end, the chordae are attached to the papillary muscles on the ventricular wall. The chordae tendinae are primarily made up of an inner core of collagen which is covered with a loosely meshed elastin and collagen. The outer surface of the chordae tendinae is covered with endothelial cells. The main function of the chordae tendinae and papillary muscle is to prevent the leaflets from prolapsing into the left atrium in the fully closed position [8].

Mitral valve stenosis, a slowly progressive disease of the mitral valve remodels the mitral valve structure into a "fish mouth" apparatus which prevents efficient filling of blood in the left ventricle. It has been observed that mitral valve stenosis is mainly associated with rheumatic fever. The pathological process leading to mitral valve stenosis observed in patients are thickening and calcification of leaflets, fusion of the commissures or chordae tendinae or the combination of the above. In infants congenital malformations of the mitral valve are responsible for stenosis. Other factors affecting the mitral valve are infective endocarditis, left atrial myxoma and mitral annulus calcification in the elderly. Treatments are aimed at alleviation of the left ventricular filling obstruction and thereby reduce the transvalvular pressure gradient. Mitral valve replacement, open or closed commisurotomy or percutaneous balloon valvotomy may be performed based on the shape of the fused mitral valve apparatus. These procedures have shown significant improvement in reduction of symptoms and the quality of life of patients.

It should also be noted that if there is a significant amount of calcification, fibrosis and fusion of the valve or presence of regurgitation, mitral valve replacement is preferred over other procedures. On the other hand, causes of mitral valve regurgitation include mitral valve prolapse secondary to myxomatous degeneration, rheumatic fever, coronary artery disease and infective endocarditis. Mitral regurgitation can also occur due to rupture of chordae tendinae. Generally mitral regurgitation is seen as a surgical disease with mitral valve repair or replacement as the treatment option. Mitral valve replacement can be done either with preservation of part or all of mitral apparatus or complete removal of mitral apparatus. The choice is made depending on the condition of the diseased valve. For example, in the absence of calcification, rheumatic involvement and the diseased leaflet happens to be the posterior leaflet, mitral valve repair is the preferred choice of treatment, thereby avoiding anti-coagulant therapy or the risk of bio-prosthetic valve failure in future. Also the shape of the mitral valve apparatus is maintained as it is considered essential for the normal functioning of the left ventricle. On the other hand, mitral valve replacement is preferred when the native valve is so distorted due to severe calcification or rheumatic fever [9].

1.2 Bio-prosthetic Valve

Prosthetic valve replacement is one of the integral treatment modalities of the valvular disease as we saw from the previous sections. While mechanical valves are highly durable, patients are required to undergo anticoagulant therapy due to the non-physiological flow presented by the mechanical valves [10, 11, 12, 13, and 14]. Flow dynamics through the bio-prosthetic valve on the other hand is very

similar to the natural valves and thus patients need not run the risk of anticoagulation therapy and its associated complications. Bioprosthetic valves are either excised porcine aortic valves or bovine pericardial tissue made in the shape of the human aortic valve. The valves are fixed in glutaraldehyde solution and are limited by its durability. It has been observed that tissue valves deteriorate in its functionality and structure with time owing to calcification, tissue degeneration and leaflet tear which often leads to stenosis or regurgitation. It has been observed that 50% of porcine aortic valve fail within 10-15 years. The failure rate in those implanted in patients less than 35 years old is reported to be almost 100 % which makes it unsuitable for younger patients [15]. Thubirkar et al [16] highlighted the role of mechanical stresses in calcification of tissue valves in the early eighties. In that study different types of bioprosthetic valves were implanted in the aortic position in calves to study the location and distribution of calcification. It was observed that highest stresses occurred in the region of greatest flexion of the leaflet, where calcifications are normally observed. In the case of porcine valves, calcification occurred earlier in the commissural region where stresses were noted to be higher than in the base. On the other hand, pericardial valve had calcification at multiple foci at areas of higher flexion. The study concluded that mechanical stresses initiate calcification by damaging the structural integrity of the tissue. In another study [17], aortic cusps from patients who underwent aortic valve replacement were examined. It was found that calcific deposits were found in the leaflet coaptation region that underwent highest flexion, i.e. region of maximal stress. This study also concluded that the mechanical stress may be the inducing

factor for calcification. For many years calcification was thought to be the main culprit in valve degeneration with leaflet tear secondary to calcification. But studies [18, 19] have shown that calcification is initiated from the phosphate rich dead cells of the fixed valve. When these dead cells are exposed to the calcium rich plasma cells, calcium phosphate minerals are formed that are deposited in the valve surface thus indicating that calcification and tearing can be two separate processes. In order to study the mechanism of tissue valve failure and the molecular mechanisms involved in the mechanical stress induced valve degeneration [20], in vitro cyclic fatigue experiments were conducted where porcine aortic valves underwent accelerated flex fatigue conditions. The study reported GAGs loss in the aortic valve cusps and reduction in bending strength caused by the cyclic fatigue. Spectroscopic studies showed that type I collagen damage also occurred due to cyclic fatigue. The above study also strengthens the view that valvular degeneration and calcification occur due to different factors. It should how ever be noted that all the above experimental studies highlight the importance of mechanical stress as one of the main instigator for valve degeneration.

1.2.1 Computational studies on tissue heart valves

An accurate computational model can be used as an excellent tool in the area of heart valve research. Computational models are economical and provide researchers and valve engineers with a means to validate heart valve performance while looking for design improvements. In a clinical setting, when combined with patient specific models obtained from various imaging techniques such as MRI and CT, computational models can help in providing real time information to improve

patient care [21].

Turn of the century has seen many developments in numerical techniques as well as computational power. This has enabled researchers to numerically simulate the dynamics of heart valves. Many simulations have been carried out as a pure structural analysis. Gyaneshwar el al [22] conducted a dynamic finite element analysis using a shell element with a linear elastic material model to study the leaflet aortic root interaction and the stress developed during a cardiac cycle. They reported that the aortic root dilation starts before the leaflet opening and contributes almost 20 % of the leaflet opening. They also observed that stress patterns were higher in the coaptation area during closure and the stress magnitude kept increasing as the valve moved toward closure. These observations highlight the fact that stresses are higher at the points of greater flexion which occurs during the coaptation process. Biological tissues are highly non-linear anisotropic materials; hence using a linear elastic material does not yield a realistic solution. In order to perform an accurate analysis, it is necessary to incorporate a physiologically realistic material into the problem. Kim el al [23] developed a stress resultant shell model with a Fung-type elastic constitutive model to represent the bioprosthetic valve leaflets. The material properties were obtained from a bi-axial test and a three point bending test. Both opening and closing was simulated in an effort to understand the dynamic stress variance during different phases of the cardiac cycle.

The results of the computational model were compared with experimentally measured data for validation. It was observed that higher stresses first appeared near the belly region during opening and then started to spread over to the free

edge area as leaflet stretched out. The highest value was seen in the middle of the free edge at fully open position. During closing the maximal stress was found in the vicinity of the commissural area with highest point at both ends of the commissures. Highlight of this study was the use of a realistic material model to represent a pericardial tissue valve. Finite element study using the Fung Material model conducted by Jermihov et al. [55] on bicuspid aortic valve to compare the opening and closing behavior of different variants of BAV geometry showed that effective orifice area during opening is significantly reduced in the case of BAV and the maximum in-plane von-mises stress on the leaflets is high compared to the normal leaflets particularly during the closing phase. Conti et al also developed a dynamic 3-D FEM model of a bicuspid aortic valve with the root geometry using image derived data. The effects of the raphe thickening on the deformation process were also analyzed. Results showed that the leaflets behaved asymmetrically during the opening phase resulting in an elliptical shaped orifice [68]. The presence of cusps increased the stress levels in one of the leaflets and the stress distribution was compared to be more in the BAV than in a normal aortic (tri-leaflet) valve.

Although pure structural analysis can yield valuable results, it is far away from reality as the effect of the presence of an ever changing complex fluid pattern is ignored. As the blood begins to flow across the leaflets, vortical structures are created which could in turn affect the way the leaflet deforms, thus necessitating FSI based analysis. FSI based on Immersed boundary method was developed by Peskin et al., [69] where the fluid is treated in the Eulerian frame and the structure is treated in a Lagrangian frame of reference. The goal of this method was to study

flow patterns around native and bioprosthetic heart valves. The interfacial effects are communicated to the flow as a body force in the momentum equation. One of shortcomings of this method was the smearing of the interface [69, 28] which affected the accuracy of the whole system as the movement of the interface affects the fluid moving around it which in turns determines the deformation of the structure. Numerical stiffness and the time step size are other problems of IB method [70].

FSI studies based on finite element method were conducted by de Hart et al on a two dimensional model of a leaflet in the aortic position [24]. The fluid solver was based on a fixed Eulerian grid and the structural solver is based on a Lagrangian grid and fictitious domain method was used to couple between the solid and the fluid. Furthermore the results of the computational model were validated using a corresponding three dimensional geometry in a pulsatile flow loop. A rubber sheet made of ethylene-propylene-diene monomer was used to simulate the leaflet for the experimental model and the corresponding material properties were applied for the computational model as well. The stiffness of the material was 300 times that of a tissue valve. The study reported flow and structural phenomena occurring differently for leaflets with different thicknesses. As predicted the thinner leaflet offered less resistance to the flow and showcased a different bending behavior as opposed to the thicker leaflet. Jet flow was observed in the gap region for both the cases and negative velocity profile in the sinus cavity. De hart et al [25] took the above study one step further by performing a three dimensional fluid interaction analysis of stented aortic valve. The aortic leaflet was represented by an isotropic

linear elastic material based on the Neo-Hookean constitutive model. The simulation was performed in the peak forward and the decelerating part of the systolic phase. It was observed that the valve motion was largely governed by the fluid motion and the opening and the closing behavior were entirely different. During opening, tensile stresses dominated on the aortic side in the mid region and the compressive stresses on the ventricular side. Due to computational limitations in building dense meshes, simulations were not performed in a realistic setting and the maximum Reynolds number was observed to be 900 whereas the realistic value for this parameter should be about 4500 to simulate physiological flow. Yet the study was able to capture some essential kinematics during the cardiac systole.

Two dimensional fluid solid Interaction study was conducted by Vigmostad et al [26] to study the opening behavior of a tissue valve in the aortic position. Locally refined Cartesian mesh sharp interface method was developed for solving the flow around deformable bodies. To compute the leaflet motion, a 2-D beam element with anisotropic non-linear material properties was used to represent the valve leaflet. In order to maintain stability of the numerical process, the fluid-solid interaction was strongly coupled as the FSI algorithm was based on a partitioned approach which will be explained in the later sections. One of the highlights of this study is that it was capable of simulating valve motions under physiological Reynolds number as the local mesh refinement algorithm was able to capture the flow features adequately meanwhile saving computational cost as well. As opposed to the two dimensional study conducted by de Hart et al [24] which used a coarse mesh, this study was able to fully resolve the flow field including the shear and the

boundary layers as the grid was very fine in the vicinity of the interface.

The previous study [26] was limited by its two dimensional setting as the tissue valves are complex three dimensional structures and get even more complex during deformation. This deformation will influence the fluid around it and vice versa thus making the analysis highly three dimensional.

1.3 Specific aims

The focus of this thesis is to implement a stable fluid structural interaction technique to simulate the dynamics of tissue valves including bio-prosthetic heart valves and natural heart valves under physiological Reynolds numbers. The goal is to capture the flow features across the deforming valve and demarcate the stressed regions during the dynamics. A partitioned approach is implemented where the equations governing the flow and the displacement of the structure are solved using two distinct solvers. The flow solver and the solid solver is strongly coupled so as to conserve the balance of momentum and energy while performing numerical studies involving similar fluid and solid densities. The roles of added mass effects that arise during such problems are also investigated. In order to fully resolve the flow, the simulations will be performed using parallel computations which enable us to use high density meshes.

The aim of this thesis is to develop a stable FSI algorithm with which we can simulate the following problems in the area of heart valve dynamics during the opening and forward flow phase of the cardiac cycle in a full three dimensional (3D) setting. These simulations will enable us to understand the effects of pathological malformations such as BAV both on the structural side as well as the variation in

flow pattern. On the other hand, applications for the mitral valve simulation include mitral valve repair, surgical planning etc. The work presented in this thesis can serve as a good platform to include contact mechanics which will enable us to perform the valve dynamics simulations during a complete cardiac cycle.

CHAPTER II
METHOD

Two main approaches exist in the simulation of fluid structural interaction. The first one is called 'monolithic' approach where the equations of flow and structure are solved simultaneously with a single solver. The second approach is called the 'partitioned' approach where we use two distinct solvers for the fluid and the structure. The flow and the structure are solved separately within a given time step with information exchanged between the solvers at the interface. In this thesis, the second method will be used as tested flow and solid solvers are already available. ELAFINT 3D which has been extensively tested and used in a number of fluid dynamic applications will be used as the fluid solver. Local mesh refinement (LMR) techniques which adapt the mesh based on the local flow dynamic complexity will be utilized to save computational cost. Solid solver based on FEAP with Newmark algorithm for dynamic structural analysis will be used to solve for the valve structures. It has been observed that the valve leaflets undergo a high degree of bending during its opening and closure. So it is imperative that this bending behavior is accurately captured to ensure the accuracy of the FSI problem in its entirety. Enhanced Assumed Strain (EAS) solid shell element has been used to represent the structure which is known for its ability to capture the bending behavior of thin structures, absence of shear and volumetric locking meanwhile maintaining coarse mesh accuracy. Equally important is the right choice of a constitutive model to describe the behavior of the valve material. To maintain the stability in partitioned approach, particularly in problems such as heart valves where the density of the fluid and the solid are of the same order, the fluid and the

solid solvers are to be strongly coupled, that is, the solution will be performed multiple times per time step. Details of the strongly coupled method will be discussed in the later sections.

2.1 Flow Solver

Capturing the flow dynamics is an important aspect when we deal with cardiovascular systems particularly when the flow conditions depict the physiological conditions and also when the problem is three dimensional. This is particularly important in 3-D FSI problems as the flow patterns determine the deformation of the solid. The flow solver will have to deal with a variety of challenges as described below:

- The goal in the present work is to simulate a FSI problem with solid that involves very large deformation which makes it a moving boundary problem. The leaflets or the embedded structure is thin and very pliant. This makes the solid response to fluid almost instantaneous [26]. The flow solver should have the capability to capture this effect without any compromise to the accuracy and remain stable though out the simulation.
- The structure in our system, i.e. the heart valve leaflets respond to the fluid forces in the form of pressure and shear [26,] which come from the fluid solution provided by the flow solver. Hence the interface forces will have to be captured accurately. In fact the accuracy of the whole solution or the simulation largely depend on the computation of the surface forces such as the interface pressure and shear which forms the traction boundary for the solid solver.

- When the goal of the problem is to analyze heart valve opening dynamics in a physiological flow conditions, this involves high Reynolds number flows [24, 25]. This along with a complex deformation that can be anticipated from the structure will present a complex flow dynamics such as boundary layer separation, high velocity jet flows during peak systole, negative flows, vortical structures and recirculation [26]. These significant flow dynamics has to be captured by the means of a high density grid for an adequate flow resolution requiring high performance computing and adaptive mesh refinement for an efficient computation

An efficient moving boundary flow solver capable of dealing with the challenges presented above has been developed in our lab in a parallel framework [71]. The massively parallelized flow solver has been specifically designed to deal with high Reynolds number flow and computationally challenging moving boundary problems. The flow solver is based on a Cartesian approach with levelset based representation of geometries. Validation of the flow solver with benchmarking problems showed that the hybridized least- squares ghost fluid Cartesian grid method is able to handle complex moving boundary problems efficiently. The parallel flow solver with local mesh refinement algorithm and mesh pruning capabilities (extraneous of the flow domain) allows us to use a very high density mesh distributed over hundreds of processors with an end result of a high flow resolution in an efficient manner [71]. A brief overview of the flow solver from Mousel [71] is presented in the following section and for more details such as an

elaborate discussion of the parallel framework and other capabilities including validation of the flow solver; the reader is referred to [71].

Cartesian Grid Method: To solve three dimensional incompressible flows around moving interface such as heart valves, a well-tested computer code called ELAFINT 3D is used. To discretize the incompressible Navier-Stokes equation, a second order accurate Cartesian grid based finite difference scheme has been employed. One of the main advantages of using a fixed Cartesian mesh as opposed to body fitted mesh in FSI algorithms that mainly uses segregated solvers is that the fixed Cartesian mesh allows the solid interface to have large deformation over it. This helps us get rid of problems related to mesh generation owing to the solid deformation that are typically needed in ALE type methods.

Governing equations: Navier-Stokes equations in their non-dimensional form are:

$$\vec{\nabla}.\vec{u} = 0 \tag{1}$$

$$\frac{\partial \vec{u}}{\partial t} + \vec{u}.\vec{\nabla}\,\vec{u} = -\vec{\nabla}\,p + \frac{1}{Re}\nabla^2\vec{u} \tag{2}$$

where $Re = {}^{\rho_f UD}/_{\mu}$ is the Reynolds number with ρ_f, U, D, μ being the fluid density, characteristic velocity, length scale and the fluid viscosity respectively. The flow variables such as the pressure and velocities are stored in the cell centers in a collocated arrangement. ELAFINT 3D employs a four step fractional step method to decouple the velocity and the pressure variables. In the first step, we evaluate an intermediate velocity field without enforcing the incompressibility constraint. That is we split equation (2) above to get:

$$\frac{\overrightarrow{u^*} - \overrightarrow{u^n}}{\Delta t} = -\vec{u}.\vec{\nabla}\,\vec{u} + \frac{1}{Re}\nabla^2\vec{u} \tag{3}$$

In the above equation, the convective term, $\vec{u}.\vec{\nabla}\,\vec{u}$ can be discretized using a second order explicit Adam- Bashforth equation.

$$-\vec{u}.\vec{\nabla}\,\vec{u} = \frac{1}{2}\left[\vec{u}^{n-1}.\vec{\nabla}\,\vec{u}^{n-1}\right] - \frac{3}{2}\left[\vec{u}^{n}.\vec{\nabla}\,\vec{u}^{n}\right] \quad (4)$$

A second order semi-implicit Crank Nicholson scheme method is applied to the diffusive term $\frac{1}{Re}\nabla^2\vec{u}$.

$$\frac{1}{Re}\nabla^2\vec{u} = \frac{1}{2Re}\left[\nabla^2\vec{u}^{*} - \nabla^2\vec{u}^{n}\right] \quad (5)$$

The resulting equation to evaluate $\vec{u}^{*}$

$$\frac{\overrightarrow{u^{*}} - \overrightarrow{u^{n}}}{\Delta t} = \frac{1}{2}\left[\vec{u}^{n-1}.\vec{\nabla}\,\vec{u}^{n-1}\right] - \frac{3}{2}\left[\vec{u}^{n}.\vec{\nabla}\,\vec{u}^{n}\right] + \frac{1}{2Re}\left[\nabla^2\vec{u}^{*} - \nabla^2\vec{u}^{n}\right] - G(q) \quad (6)$$

In Equation (6) G (q) is a suitable estimate for the pressure gradient.

The second step involves in removing the estimate of pressure gradient.

$$\overrightarrow{u^{**}} = \overrightarrow{u^{*}} + G(q)\Delta t \quad (7)$$

Incompressibility is now enforced by decomposing $\overrightarrow{u^{**}}$ into sum of divergence free and irrotational vector fields.

$$\vec{u}^{n+1} = \overrightarrow{u^{**}} - \Delta t\nabla\varphi \quad (8)$$

By taking the divergence of the above equation and also requiring a divergence free velocity $\vec{u}^{n+1}$, a Poisson equation for the scalar potential φ as shown below

$$\nabla^2\varphi = \frac{\nabla.\vec{u}^{**}}{\Delta t} \quad (9)$$

Discretization of the operators is done using finite difference schemes and the details can be found at [71].

Levelset Field: The Interface or the moving boundary (valve leaflets in our case) is represented by levelsets. The levelset field is a signed normal distance computed from a grid point that belongs to a surface mesh. The surface mesh itself represents the zero iso-contours that is the at the surface mesh, $(\vec{x}, t) = 0$. The application of the boundary conditions and solving for velocity and pressure are done at the zero levelset location [28]. The normal distance is defined to be negative inside of the surface and positive in its exterior. The levelset field is governed by the levelset advection equation given below

$$\phi_t + \vec{V}.\nabla\phi = 0 \tag{10}$$

Here $\vec{V}$ is the levelset velocity field which is determined by the physics of the problem. In this present case, the velocity of the leaflet surface (where$\phi(\vec{x}, t) = 0$) is obtained as a solution from the solid subdomain. The Interface velocity thus obtained is extended along the normal direction to define the propagation velocity to rest of the domain. The levelset advection equation (equation 10) is solved using a third order Runge – Kutta time stepping scheme and for the spatial discretization, a 5th order WENO upwind scheme is used. The levelset is calculated and stored in a narrow tubular grid around the interface to save computational time and this tube is rebuilt so as to prevent the zero levelset from moving out of the domain over which it is computed. New points are introduced to the band and are initialized with the levelset re-initialization equation given in equation (11).

$$\frac{\partial\phi}{\partial\tau} + sign(\phi)\vec{n}.\nabla\phi = 0 \tag{11}$$

In the above equation τ represents pseudo time and the solution process is continued until steady state and once the convergence is attained, the levelset field

satisfies the normal distance property $|\nabla\phi| = 1$ with valid values given to the newly initiated points.

Computation of Surface forces: In our present case, the solid solver gets the pressure and shear load from the fluid solver and deforms to the traction. This necessitates a smooth and a stable method to compute the surface forces. In the current framework, a least square based method is used to evaluate the surface forces by fitting a polynomial of arbitrary order to the nearest fluid points surrounding the interface location [71]. The process is briefly explained below.

Let x_{int}, y_{int} and z_{int} be the interface location, and then the polynomial fit about the interface location is of the form

$$\psi = a_\psi + b_\psi x_r + c_\psi y_r + d_\psi z_r + e_\psi x_r y_r + f_\psi x_r z_r + g_\psi z_r y_r + h_\psi x_r^2 + i_\psi y_r^2 + j_\psi z_r^2 \tag{12}$$

Where $x_r = x - x_{int}, y_r = y - y_{int}, z_r = z - z_{int}$

The expansion coefficients are determined for pressure and each component of velocity and using that the stress tensor at the interface is formed as given below

$$T|_s = -p|_s I + 2\mu D|_s = -a_p I + \begin{bmatrix} 2\mu b_u & \mu(c_u + b_v) & \mu(d_u + b_w) \\ \mu(c_u + b_v) & 2\mu b_v & \mu(c_w + b_v) \\ \mu(d_u + b_w) & \mu(c_w + b_v) & 2\mu b_w \end{bmatrix} \tag{13}$$

Here $p|_s$is the pressure at the surface and $D|_s$is the deformation rate tensor.

The pressure and shear force thus obtained will be used as the traction boundary condition for the solid subdomain.

Local Mesh Refinement: In order to capture the significant flow dynamics of the flow field in the vicinity of leaflet such as the shear and the boundary layer it is often required using a high density mesh in these regions. Instead of using a uniform high

density Cartesian mesh that would increase the computational cost, ELAFINT 3D employs a local mesh refinement (LMR) technique to enhance efficiency and simultaneously save time [10]. When LMR is used, the mesh is automatically refined (a single Cartesian cell is divided into many smaller cells based on the levels of refinement required) and coarsened based on specified criteria such as gradients of flow. The mesh is automatically refined at regions of high flow gradients, for example, the vicinity of the leaflet surface and other regions where the boundary layer are significant. Also the mesh is coarsened at regions where the flow is fairly uniform and at regions which are not of interest thus saving time and cost. ELAFINT with LMR has been employed in many studies [10, 11, 12, 13, 14, 26] involving the fluid structural interaction of mechanical heart valves and tissue valves. It has been reported that LMR has substantially improved the performance of the flow solver to many fold. As discussed in the previous sections, the goal of the present study is the simulation of heart valves under physiological conditions. It has been observed in several studies [29, 30] that physiological Reynolds number for blood flow in aorta during peak systole is more than 4500. Thus the flow can be expected to be predominantly laminar with brief transitional behavior during the deceleration phase at the end of the opening phase in aortic flow. In order to capture this complex flow dynamics, a very high density mesh needs to be available at regions of high flow gradients. . Employment of LMR in such a situation becomes almost a necessity for efficient and accurate computation.

2.2 Modeling Blood as a Newtonian Fluid:

It is important to consider the rheological properties of blood when setting up a fluid structural interaction problem involving heart valves. It has been shown that blood behaves differently as it flows through different blood vessels. Formed elements constitute 45% by volume of the whole blood (of which 95% are red blood cells ; 0.13% white blood cells; and 4.9% platelets). The remaining 55% of the whole blood is made up of plasma which has fibrinogen, globulin, albumin and water. These different constituents have their own viscous behaviors under different conditions. Although plasma primarily consists of water, the presence of plasma proteins increases its viscosity. Studies have reported that plasma behaves as a Newtonian fluid [Whitmore, 1968] with constant viscosity at a given temperature. Viscosities of the whole blood have known to change under the different rates of shear. At low shear rates, apparent viscosity of blood tends to be higher but as shear rates exceed 50 sec^{-1}; viscosity decreases and reaches an asymptotic value of 3.5 cp. For most of the cardiac cycle the shear rates are observed to be more than 50 sec^{-1} in major arteries and the chambers of the heart and hence blood can be assumed to be Newtonian while performing fluid simulations [8, 10, 11, 12, 13, and 14].

2.3 Solid Solver with Enhanced Assumed Strain Solid Shell Element

For the analysis of nonlinear problems, a coupled system of P.D.E's namely, kinematical relations, local balance of momentum and the constitutive equations have to be solved simultaneously. These equations are shown below in their strong form in the initial configuration [31].

Kinematics: $$E = \frac{1}{2}(F^T F - 1) \quad (14)$$

Equilibrium: $$Div(FS) + \rho_0 \bar{b} = \rho_0 \dot{v} \quad (15)$$

Constitutive equation: $$S = \frac{\partial w}{\partial E} \quad (16)$$

E is the Green-Lagrangian strain measure and F is the deformation gradient. S is the second Piola-Kirchhoff stress. $\rho_0 \bar{b}$ describes the volume force and $\rho_0 \dot{v}$ is the internal force.

Heart valves undergo high rate of deformation during its opening and closing. One of the main challenges of the solid solver is to capture this complex motion during the solution process. Adding to the complexity is the high aspect ratio of the leaflet. For example, the radius of the leaflet is more than 1.5 centimeters and the thickness is approximately 200 micrometers. The leaflet geometry as well as its property is highly non-linear as well. All the above challenges should be properly dealt with on the structural side in order to simulate an accurate fluid structural interaction problem involving heart valves.

2.4 Enhanced Assumed Strain Solid Shell element

L. Vu-Quoc and X.G Tan [32, 33] formulated a simple lower order solid shell element which allows efficient and accurate analysis of large deformation shell structures originally meant for composite layers. The element called EAS (Enhanced Assumed Strain) Solid shell element had a superior performance when compared to solid elements. The EAS element has only displacement degree of freedom (DOF) which makes it easy to implement when compared to shell elements which has both displacement and rotational DOFs. It is based on mixed Hu-Washishu variational principle which leads to enhanced strain parameters which was originally proposed

by Simo and Rifai [34]. This method improves the in-plane and out- of plane bending behavior by eliminating the volumetric locking. To get rid of the transverse shear locking and thickness locking effects, assumed natural strain has been combined with the above formulation. Numerical test conducted by the authors showed that the EAS element was efficiently able to capture large deformation in structures with high aspect ratio at a good accuracy. These abilities make EAS solid shell element a good fit for representation of valve leaflet for our FSI problem.

In order to overcome the problems with the rotational degrees of freedom with the shell elements, Vu-Quoc and Tan [32, 33] described the deformation using the position vectors of a pair of material points at the top and bottom surface of the shell surface. This description enables us to use the standard 8 node brick element. The Green Lagrangian strain tensors are expressed in terms of convective coordinates as follows.

$$E^c = \frac{1}{2}\left[g_{ij} - G_{ij}\right]G^i \otimes G^j = E^c_{ij} G^i \otimes G^j \tag{17}$$

Where the individual components of E_{ij} can be computed as:

$$E^c_{ij} = \begin{bmatrix} E11 \\ E22 \\ E33 \\ 2E12 \\ 2E13 \\ 2E23 \end{bmatrix} = \begin{bmatrix} 0.5(g_{11} - G_{11}) \\ 0.5(g_{22} - G_{22}) \\ 0.5(g_{33} - G_{33}) \\ (g_{12} - G_{12}) \\ (g_{13} - G_{13}) \\ (g_{23} - G_{23}) \end{bmatrix} \tag{18}$$

One of the popular methods to tackle shear locking is the assumed natural strain Method proposed by Dvorkin and Bathe [35]. This method is widely used in situations where the mesh is severely distorted or the analysis involves a thin

structure like heart valves. In the case of shear locking, it has been observed that even EAS method doesn't perform very well, which calls for the implementation of the ANS technique.

Assumed Natural strain technique works by assuming the transverse shear strains in the isoparametric space. In our conventional method, we derive the strains directly by the interpolation of displacements as we saw in the previously. In addition, the transverse strain field is also interpolated to counter act the shear locking. Hence the interpolation of the displacement and the transverse strain field are performed in this method. In other words, In order to define an ANS element, we need to specify the nodes and the corresponding shape functions of the displacement functions, which form the basis of the conventional method. Secondly the number and the location of the sampling points (which could be the region defining the mid-surface of the hexahedral element as shown in figure 1) and its shape functions for interpolating the transverse strain fields. The interpolated strain fields are given as follows.

$$E_{ANS} = \begin{bmatrix} 2\widetilde{E_{13}} \\ 2\widetilde{E_{23}} \end{bmatrix} = \begin{bmatrix} (1-\xi^2)\mathrm{E}_{13(\mathrm{A})} + (1+\xi^2)\mathrm{E}_{13(\mathrm{C})} \\ (1-\xi^1)\mathrm{E}_{23(\mathrm{B})} + (1+\xi^1)\mathrm{E}_{23(\mathrm{D})} \end{bmatrix} \tag{19}$$

Where $\mathrm{E}_{13(\mathrm{A})}$,$\mathrm{E}_{13(\mathrm{C})}$,$\mathrm{E}_{23(\mathrm{B})}$,$\mathrm{E}_{23(\mathrm{D})}$ are natural shear strains located at points ACBD situated on the mid-surface of the solid element as represented in figure and as described above, the ANS is interpolated as represented in the below figure.

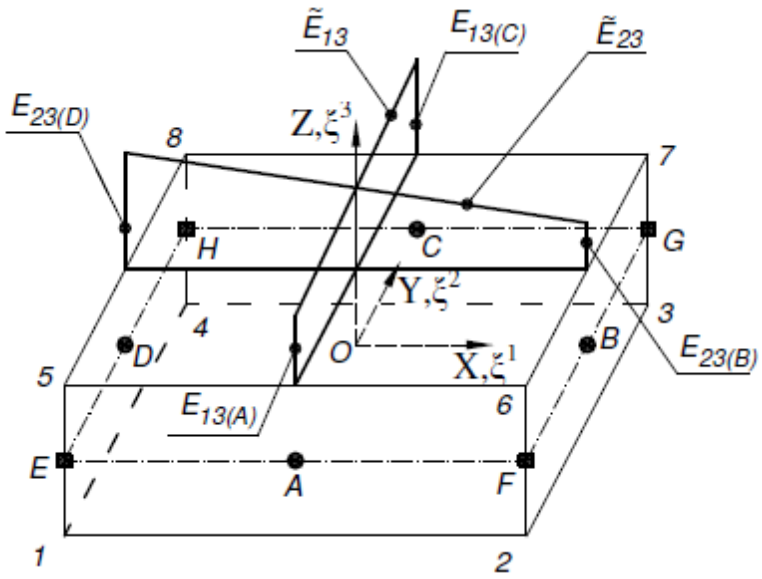

Figure 1: Implementation of the ANS method

In order to alleviate the shear locking effects, the natural strains E_{13} and E_{23} are replaced by assumed natural shear strains $\widetilde{E_{13}}$ and $\widetilde{E_{23}}$ before we do the transformation of the strain components from the isoparametric space to the Cartesian space. If T^{-T} represents the transformation matrix, the Final strain field after ANS implementation can be written as equation 9 and the strain displacement matrix is shown in equation 10. Note that all other strain components are retained except E_{13} and E_{23}.

$$\check{E}^{ANS} = T^{-T} \begin{bmatrix} E11 \\ E22 \\ E33 \\ 2E12 \\ 2\widetilde{E13} \\ 2\widetilde{E23} \end{bmatrix} \tag{20}$$

$$B_{ANS} = T^{-T}\begin{bmatrix} N_{I,1}g_1^T \\ N_{I,2}g_2^T \\ N_{I,3}g_3^T \\ N_{I,1}g_2^T + N_{I,2}g_1^T \\ \frac{1}{2}(1-\xi^2)(N_{I,1}g_3^T + N_{I,3}g_1^T)_A + \frac{1}{2}(1-\xi^2)(N_{I,1}g_3^T + N_{I,3}g_1^T)_c \\ \frac{1}{2}(1-\xi^2)(N_{I,2}g_3^T + N_{I,3}g_2^T)_A + \frac{1}{2}(1-\xi^2)(N_{I,2}g_3^T + N_{I,3}g_2^T)_c \end{bmatrix}$$

$$Where\ I = 1\ to\ 8 \tag{21}$$

Under the frame work of EAS approach as proposed by Simo and Rafi, The enhanced strain field, is given as in equation 11. The Introduction of the enhanced strain field has been known to alleviate the problems related with volumetric locking

$$E^{enh} = \frac{|J_o|}{|J|} T_o^{-T} M_{\{\xi\}} \alpha \tag{22}$$

Where J_o is Jacobian matrix at the center of the element, J is the Jacobian. Presence of $|J_o|/|J|$ enforces the orthogonality condition which is essential for the formulation to pass the patch test. T_o is the transformation matrix at the element center and M is the enhancing matrix which enhances the normal and the shear strains. α is the internal parameter whose value vary with the number of integration points. Otherwise the values can be obtained by the mapping of the natural and the physical space. The enhanced strain field is then combined with E^{ans} of equation 9 as shown below. The modified strain field is used for further computations at the element level.

$$E^{mod}=E^{ans}+E^{enh} \tag{23}$$

The Assumed natural strain method together with the incorporation of the Enhanced strain field thus alleviates the element from transverse shear locking, curvature locking and volumetric locking. With the above strain parameters, the algorithm for the solid shell can now be implemented as given below.

1. Initialialize: k=0;$\Delta u_k = 0; \propto_k = 0; U_n$

2. Update at Element level for k+1:

Nodal displacements; $u_{k+1} = u_k + \Delta u_k$

EAS parameters $\propto_{k+1} = \propto_k - \left[k_{\propto\propto(k)}\right]^{-1}(k_{\propto u}\Delta u_k + f_{enh(k)})$

3. At element level, for each Gaussian Integration point:

a. Compute Green Lagrangian strain, $E^{c(k+1)}$

b. Assumed Natural Strain, $E^{ANS(k+1)}$

b1. Strain Displacement, $B^{ANS(k+1)}$

c. Enhanced Strain, $E^{enh(k+1)}$

d. Modified Strain, $E^{mod(k+1)} = E^{ANS(k+1)} + E^{enh(k+1)}$

e. $S_{k+1} = \frac{\partial W_s}{\partial E_{mod(k+1)}}$

Compute the Tangent matrices and the internal forces

$$k_{uu(k+1)} = k_{mat(k+1)} + k_{geo(k+1)} = \int_v (B^T\ {}^4C\ B)dv + \int_v (B^T{}_{,u}S)dv$$

$$k_{\propto u(k+1)} = \int_v (\Gamma^T\ {}^4C\ B)dv;\ k_{\propto\propto(k+1)} = \int_v (\Gamma^T\ {}^4C\ \Gamma)dv$$

$$f_{int(k+1)} = \int_v (B^T S)dv;\ f_{enh(k+1)} = \int_v (\Gamma^T S)dv$$

$$f_{ext(k+1)} = \int_v N^T b\ dv + \int_A N^T t\ da$$

Update k and f at element level

$$k_{T(k+1)} = k_{uu(k+1)} + [k_{\propto u(k+1)}]^T [k_{\propto\propto(k+1)}]^T k_{\propto u(k+1)}$$

$$r_{(k+1)} = f_{ext(k+1)} - f_{int(k+1)} + \left[k_{\propto u(k+1)}\right]^T + [k_{\propto\propto(k+1)}]^{-1} f_{enh(k+1)}$$

Save EAS Arrays: $\left[k_{\propto u(k+1)}\right]^T, [k_{\propto\propto(k+1)}]^{-1}, f_{enh(k+1)}, \propto$

4. Assemble Global Matrix K_{k+1}, R_{k+1}

5. Solve for the incremental displacement

$$\Delta U_{k+1} = {K_{k+1}}^{-1} R_{k+1}$$

2.4.1 Constitutive model

As discussed in earlier sections, various research groups have employed different constitutive model to represent the material properties of the valve leaflet. For example, Gyaneshwar el al [22] and de hart et al [24, 25] employed a linear elastic constitutive model in their aortic valve analysis. In order to raise the level of accuracy of a structural problem, the constitutive model will have to be as accurate as possible as they describe the macroscopic behavior of the material where we consider the functional dependence of the stress with respect to the motion. Bio-Prosthetic heart valves are known to exhibit a highly complex behavior that cannot be described by a linear elastic constitutive model. Researchers have examined the behavior of a bioprosthetic valve under in-plane strain and shearing using a bi-axial testing device [36, 37, 38]. Using the above experimental data, constitutive model can be constructed that describe the in-plane behavior of the leaflet. To capture the behavior in the third direction, i.e. bending, data from the flexural tests conducted on the leaflet [39] can be incorporated thus providing a fully experimental derived material model to describe the complex behavior of the bio-prosthetic heart valve

leaflet. Based on the above works, a Fung type constitutive model has been implemented in the current solid solver. Fung type material model, but with fewer parameters were also employed in the study conducted by Kim et al [23].

The general Fung type equation:

$$W = \frac{c}{2}[e^q - 1] \tag{24}$$

Where W is the strain energy function in the second Piola- Kirchhoff stress, $S = \frac{\partial w}{\partial E}$ and q is the quadratic term which characterizes the in plane shear response and is given by

$$Q = A_1E_{11}^2 + A_2E_{22}^2 + A_3E_{11}E_{11} + A_4E_{12}^2 + A_5E_{11}E_{12} + A_6E_{22}E_{12} \tag{25}$$

The C in equation 13 and A_i in the equation 14 are the material constants obtained from the bi-axial tests. Additional parameters can be incorporated from the flexural tests so that the model can extended in the third direction as well. Thus Q is represented as shown in the below equation.

$$Q = A_1E_{11}^2 + A_2E_{22}^2 + A_3E_{11}E_{11} + A_4E_{12}^2 + A_5E_{11}E_{12} + A_6E_{22}E_{12} + A_7E_{11}E_{13} + A_8E_{33}E_{13} + A_9E_{33}^2 \tag{26}$$

2.4.2 Element Test

To test the element, a cantilever beam problem was performed as suggested by Simo and Rifai [34], L. Vu-Quoc and X.G Tan [32]. The cantilever is subjected to an end load and test was conducted with two different meshes. The elements of the first mesh are uniform and regular whereas the second mesh contains highly skewed and distorted elements as shown in figure 2. Both the meshes were subjected to same loading and the bending of the two cases was compared.

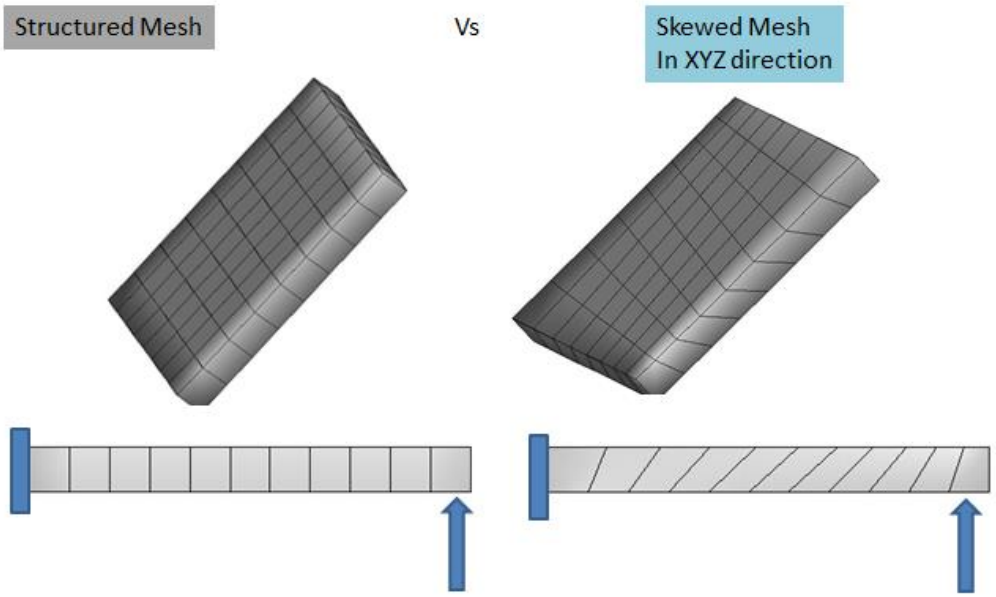

Figure 2: Mesh of Cantilever beam cases for testing mesh insensitivity.

The material used was Fung orthotropic as described in the previous section. Figure 3 shows the final deformed structure and the displacement in the Y and Z direction. It can be observed that the final deformation of both the cases are in good agreement showing the same accurate results and thus suggesting insensitivity to mesh distortion.

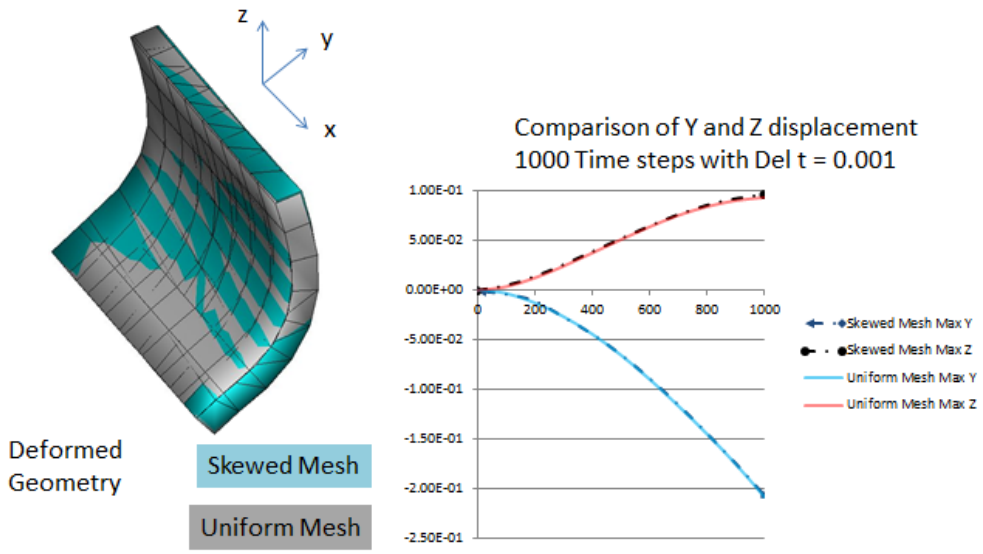

Figure 3: Comparison of deformation from the skewed and uniform mesh that shows the solution is insensitive to mesh distortion.

2.4.3 Coupling

As we saw in the previous sections, we are using two distinct solvers for the fluid and solid and the solid dynamics of the valve are computed independently of the fluid solvers using finite element methods. The fluid solver uses a fixed Cartesian mesh that allows large deformation of solid to occur over it thus liberating the fluid mesh from conforming to the solid motion. This enables us to avoid the problems related with the management of mesh generation to solid deformation.

The coupling between the structure and the fluid subdomain is enforced at the interface r_{sf}.The coupling is done with kinematic and dynamic matching conditions specifying the position of the interface at the fluid side. The continuity of the velocities at the interface is also maintained.

Let $\varphi(\vec{x},t)$ be the levelset field. Note that $\varphi(\vec{x},t)=0$ represents the interface location. Thus

$$\varphi(\vec{x},t)=0=\vec{x}|\mathrm{r}_{sf} \tag{27}$$

where $\vec{x}$ is the position of the solid obtained from the solid solver. The interface velocity and acceleration is thus given by

$$\overrightarrow{U_f}|\mathrm{r}_{sf}=\dot{\vec{x}}|\mathrm{r}_{sf} \tag{28}$$

$$\overrightarrow{a_f}|\mathrm{r}_{sf}=\ddot{\vec{x}}|\mathrm{r}_{sf} \tag{29}$$

Thus the position of the solid surface, its velocities and accelerations enter the fluid solver as inputs and serve as a boundary condition for embedded solid in the fluid solver as described in Marella et al [41]. In turn, the flow solver provides information pertaining to the forces that act on the solid surface, such as pressure to the solid solver which result in deformation. To compute the Interfacial pressure from the surrounding fluid, an implicit scheme has been devised to compute the value of pressure at the solid surface as described in [42].To briefly describe the method, The interfacial pressure is expressed in terms of other computational cells in its vicinity. This is done by extending a normal from an interfacial point and finding the intersection with the lines connecting the cell centers. The Interfacial pressure is then obtained by interpolation from the two cells from which the connecting line was drawn from their respective cell centers.

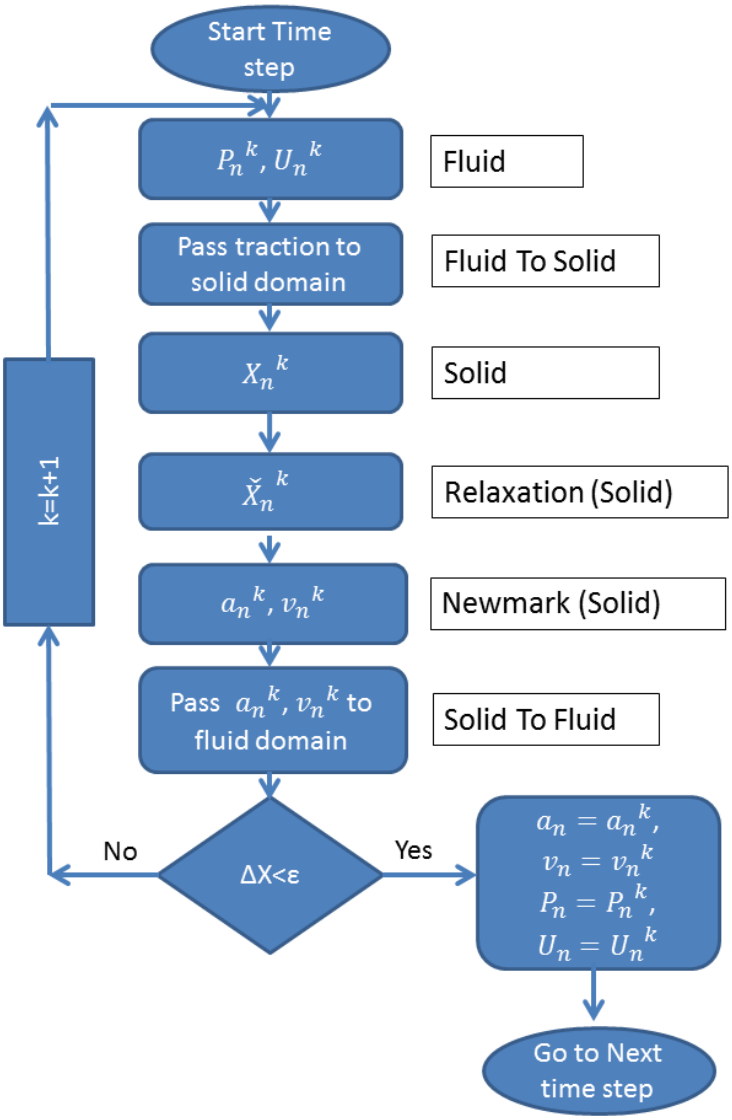

Figure 4: Flow chart of the strongly coupled FSI Algorithm

As mentioned previously, subiterations are performed in order to deal with the instability caused by strong coupling of the fluid and the solid. The convergence of the subiteration procedure in a partitioned FSI approach is heavily dependent on the strength of the coupling and the response time scale [42] as the coupling might

be sensitive to the solid deformation. There are various methods by which the subiteration schemes can be accelerated using relaxation methods. During under relaxation of the solid deformations, the computed displacements are weighted with the solution from the previous iteration to achieve the under relaxed solution. Methods vary from using a fixed relaxation parameter which is perhaps the simplest form of under relaxation procedure. As we use a constant under relaxation parameter, this method can work against the convergence and could lead to more number of iterations. This is mainly because the under relaxation parameter is heavily problem dependent [61].

In the present work, under relaxation is performed using Aitken acceleration which uses solutions from the previous two iterations to improve the current solution. This relaxation was proposed by Aitken [62] and later improved by Irons and Tuck [63]. Aitken method is very popular in dealing with FSI problems and has been implemented in numerous studies [61, 64, 65, and 66]. Present work implements the Aitken relaxation as implemented by G.E Karniadakis et al. [65] and the method is briefly described below.

The under relaxation parameter, ω_k is computed at every subiteration. The relaxation parameter is set to range between 0 and 1 as suggested by G.E Karniadakis et al [65].

$$\omega_k = \omega_{k-1} + (\omega_{k-1} - 1)\frac{(Q_{k-1} - Q_k).Q_k}{||Q_{k-1} - Q_k||^2} \tag{30}$$

$$\tilde{x}_k^n = \omega_k \tilde{x}_{k-1}^n + (1 - \omega_k) x_k^n \tag{31}$$

$$\tilde{v}_k^n = \omega_k \tilde{v}_{k-1}^n + (1 - \omega_k) v_k^n \tag{32}$$

2.5 Validation of FSI Algorithm

For validation of the strongly coupled FSI algorithm described in the previous section, a test case was chosen which was first proposed by Nuemann et al [66] and later used by S.R. Idelsohn et al [60] for the purpose of testing a FSI problem with strong added mass effect. A flexible solid flap is placed in a channel with a gradual contraction. The motion of the flap is driven by the fluid force. Both two dimensional and three dimensional studies were conducted by Idelsohn et al. [60] and the solid flap is represented by a rubber material. As the interest is with three dimensional simulations, only the 3-D version of study was used for validation in the present work. The fluid used is silicon oil with density of 956 Kg/m^3 and a viscosity of 0.145 kg/ (ms). The Young's modulus and the Poisson's ratio were 1.3E+06 N/m^2 and 0.3 respectively. The density ratio between the solid and the fluid was chosen to be 1.5 which requires a strongly coupled FSI Algorithm. The boundary conditions and the geometric configurations were same as specified by Idelsohn et al [60].

In the present study, St. Venant Kirchhoff model [67] was used to represent the material. This material model is a simple extension of the linear elastic model in the nonlinear regime. The constitutive equation is given in the equation below

$$S = \frac{\partial W}{\partial E} \tag{33}$$

$$W = \frac{1}{2} E^T D E \tag{34}$$

S is the second Piola Kirchhoff stress, W is the strain density function, E is the Green Lagrangian strain and D the elastic tangent modulus. This material was chosen mainly because the second Piola Kirchhoff stress is the work conjugate of the Green

Lagrangian strain which is the same in the enhanced assumed solid shell element routine used in the solid solver.

Initially the flap deforms to the fluid forces and the maximum tip displacement is reached near 10 seconds when the velocity also attains its maximum. Figure 5 shows the velocity contours obtained from the present validation study and figure 6 shows the local mesh refinement performed dynamically during the simulation. Both the studies noted that the maximum deflection of the plate occurred at a time when the velocity reaches the maximum value at the inlet and negative velocities behind the flexible flap. In our study, the fully developed Reynolds number was computed to be approximately 100 as was observed by Idelsohn et al as well. It was observed by Idelsohn et al [60] that, once the velocity reached its maximum value at 10 sec, which also corresponds to the maximum deflection of the plate, the plate started to retract. This recoil continued until the system reached a steady state position as shown in figure 7. Comparing the tip deflection of the flap in both the studies (Figure 7 and 8), the tip displacement was similar until 10 seconds (until the maximum velocity was attained) and after that it appeared as if the flap in the present study started to behave stiffer.

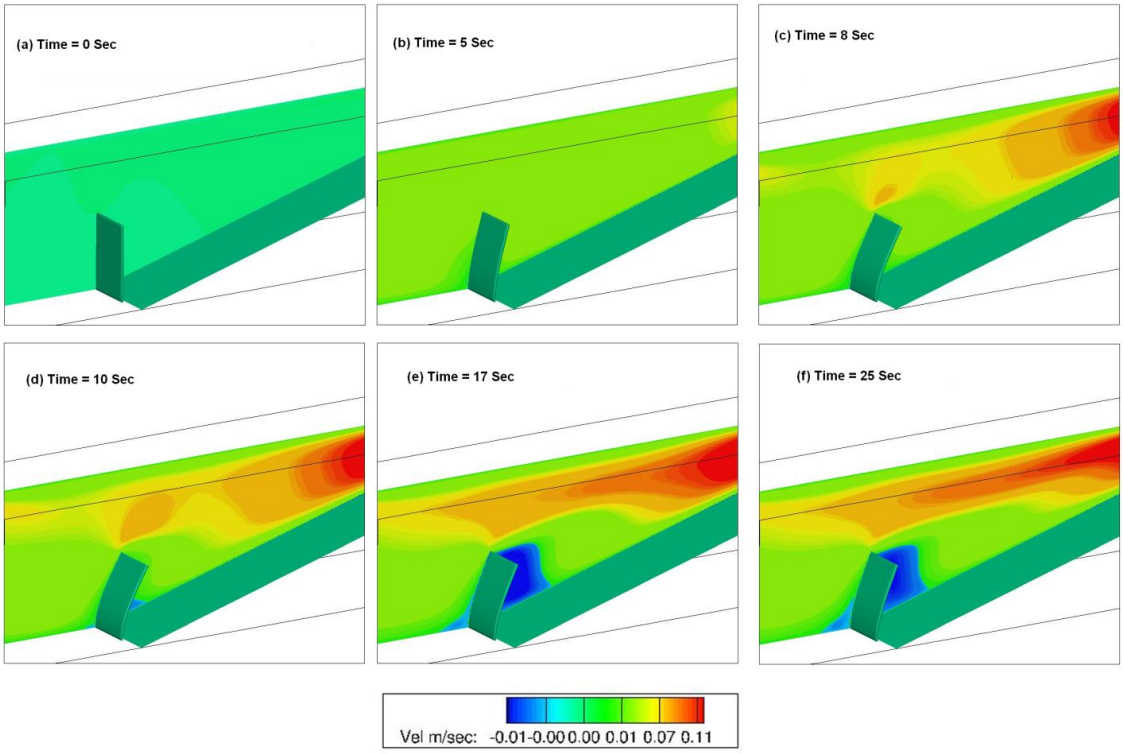

Figure 5: Velocity contours at various stages of simulation of the flexible flap in a converging channel used for validation of the FSI Algorithm.

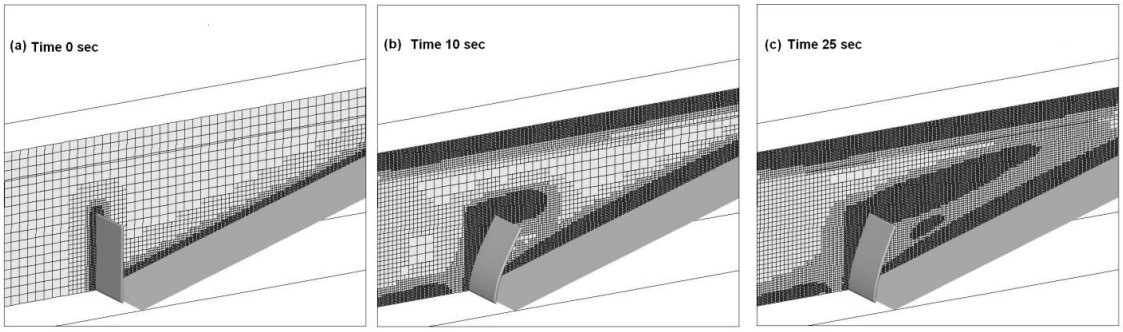

Figure 6: Local mesh refinement updates the mesh based on flow gradients without any user intervention

Although a fair comparison can be drawn qualitatively between the flap behavior post 10 seconds, such as flap retraction and an eventual steady state achievement, the magnitude of the flap retraction in the present study was observed to be lesser than that observed by Idelsohn et al [60]. This could be due to the use of a nonlinear element routine and a nonlinear material model in the present study and an elastic solid used by Idelsohn et al [60]. This difference needs further investigation and will be explained in the later sections.

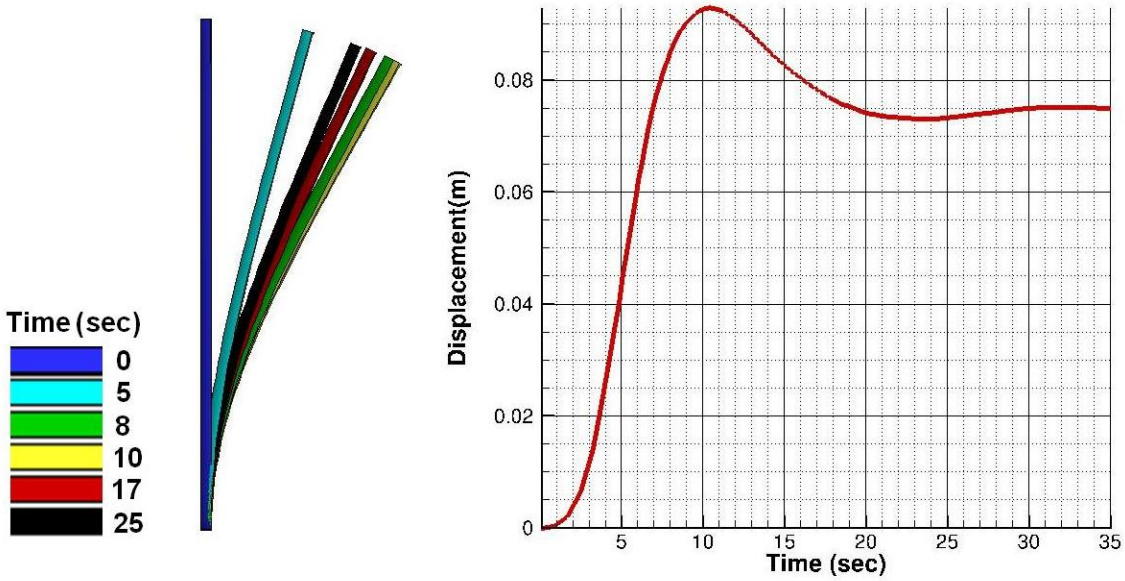

Figure 7: Stages of displacement color coded by time. Figure on the right panel shows the tip displacement as a function for time

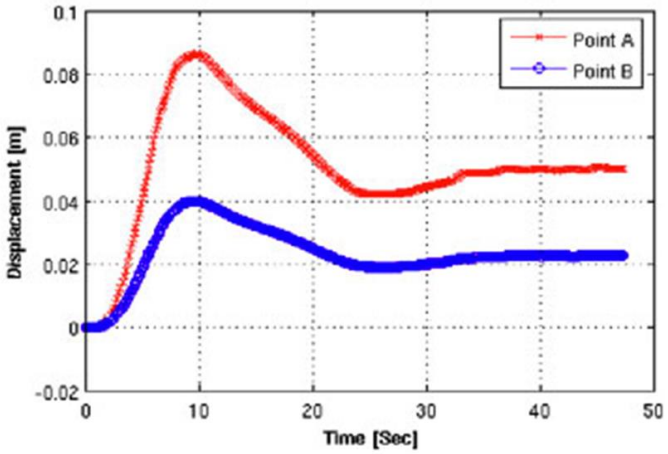

Figure 8: Results of flap displacement versus time obtained by Idelsohn et al. [60] for comparison with the present study.

Even though an identical flap behavior could not be established or emulated in the present study until steady state, we were able to capture the some of the important dynamics of a tightly coupled fluid structural interaction problem where the density ratio between the solid and the fluid was close to 1. The results showed good agreement with during the initial stages until the flap reached its maximum displacement and a similarity in overall dynamics of the system. Figure 9 shows the plot of subiteration numbers taken per time step for the entire duration of study. We can observe that the number of subiteration taken is high during the initial stages where acceleration on the solid system due to fluid is high and also between time steps 400 and 600 which correspond to time 6 and 12 sec during which the flap reaches its maximum displacement and starts to retract. We can also note that

the number of subiteration taken during the steady state is small and remains almost constant.

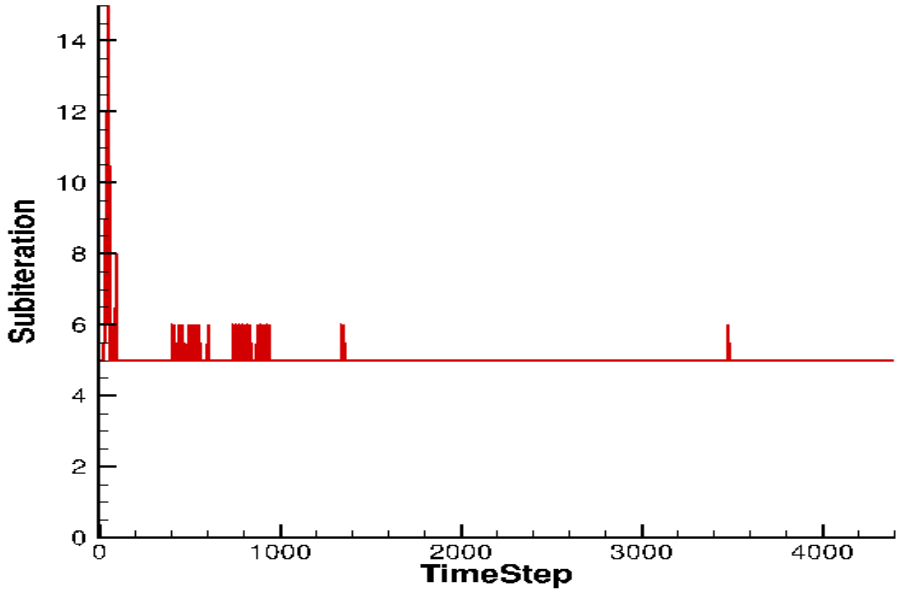

Figure 9: Subiterations are performed with in a time step in order to deal with the instability due to the tightly coupled system

CHAPTER III
FLUID STRUCTURAL INTERACTION OF PERICARDIAL BIOPROSTHETIC VALVE

Fluid structural Interaction can provide us with an understanding of both the fluid dynamics and the solid deformation during the functioning of heart valve. A three dimensional FSI study of a pericardial valve geometry is performed in order to understand the dynamics of its opening phase. The dimensions of the leaflet and the sinus cavity are chosen from the three dimensional study conducted by de Hart et al [25]. In a typical pericardial BHV the leaflets are attached to a mount as showed in the photograph in figure 10 (a) which in turn is sutured to the aortic root. In the current study the leaflets are attached directly attached to the aortic root to simplify the model. The three leaflets are assumed to have identical shapes but all three leaflets are included in this simulation to analyze the behavior of individual leaflet deformation and its effect on flow. The ventricular side (bottom surface) is defined as the inlet and a time varying axially uniform velocity is fed at the inlet. The inlet is elongated to avoid boundary influences. The aortic side forms the outlet. The rest of the surfaces are defined as walls where no-slip condition is enforced. All degrees of freedom are restricted along the edges where the leaflet is connected to the aortic root and the free edge is free to move. The regions of interest are marked as shown in figure 10(c). The simulation conditions specified above is typical of an opening of an aortic valve.

The mesh is locally refined using a local mesh refinement algorithm previously discussed to achieve a good flow resolution. This helps us to capture the boundary layers that develop at the aortic walls and also from the leaflet edges.

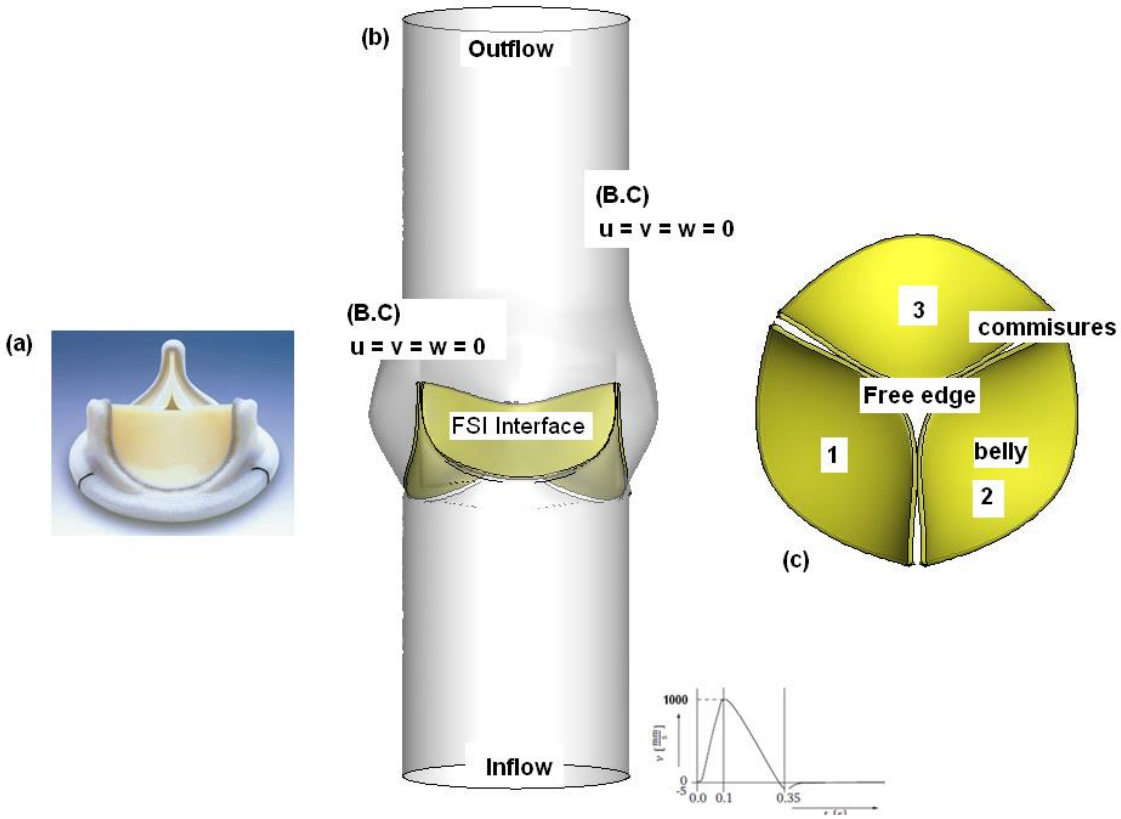

Figure 10: Details of the pericardial bio prosthetic valve simulation (a) Shows a photograph of a typical bioprosthetic valve. (b) Geometry and boundary conditions used in this study. Dimensions are obtained from an FSI study conducted by de Hart et al. (c) shows the leaflet from the aortic view with regions of interest marked.

This could be important during the late opening stages of the aortic valve where the Reynolds number could go as high as 5000. The leaflet structures are discretized into 4000 enhanced assumed solid shell elements with one element across the thickness. In the study conducted by de Hart el al, the leaflet structures are discretized using 270 structural elements with one element across the thickness. Using a fine FE mesh ensures accurate structural solution as well as a proper generation of levelsets to represent the interface for the fluid.

The three flexible leaflets of the bioprosthetic valve are described by Fung material model with material constants are obtained from a previous study which investigated the effect of different material constants using finite element study [23].

3.1 Results

The ratio of fluid to solid response time scale for bioprosthetic valve was computed to be around 40 by Vigmostad et al [26]. This means that the response of the structure to fluid is 40 times quicker than the solid or can be thought as almost instantaneous. Because of the high response time scale, the deformation can be anticipated to be very fast. This behavior can be observed from the results presented in this study.

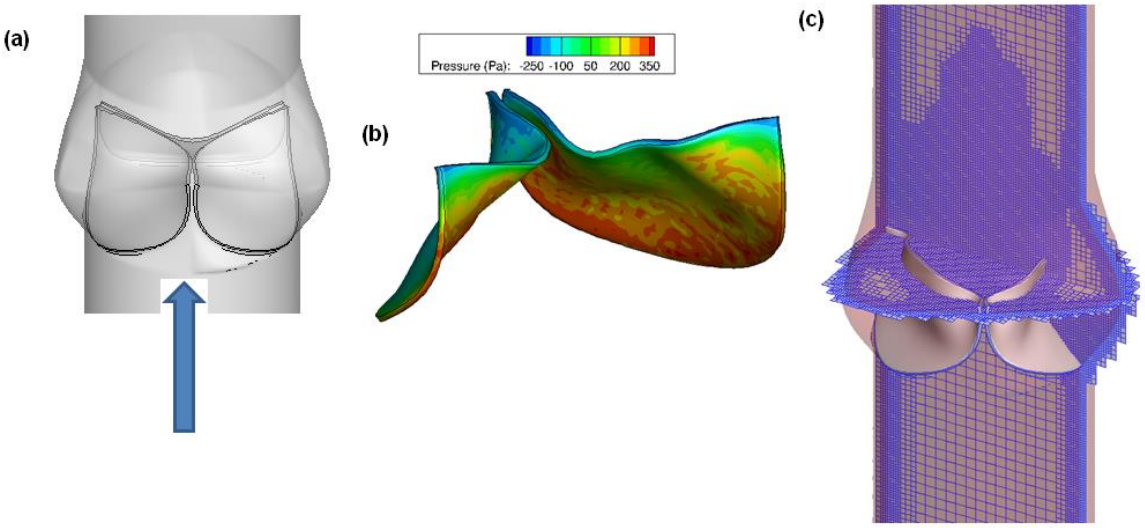

Figure 11: Initial configuration of the valve (a) leaflets are in fully closed position. (b) Interfacial pressure contours in Pascal at 0.017 sec. (c) Local mesh refinement refines mesh at regions of high flow gradient

The valve in the initial configuration is showed in Figure 11 (a). Pressure build up on the ventricular side of the leaflet causes the valve to respond to the force passively. The interfacial pressure computed from the fluid which acts as the dominant force on the leaflet. Because of the configuration of the leaflet, the pressure build up is higher on the belly of the leaflets than compared to the free edges as shown in figure 11(b). In fact the magnitude of pressure acting on the belly was noted to be three times compared to the pressure on the leaflet edge at 0.017 seconds. This causes the belly to deform relatively faster than the free edges resulting in a slight bulge and the valve starts opening by changing the curvature of the free edge. In order to achieve an adequate flow resolution, local mesh refinement algorithm automatically refines the computational domains in regions of high flow gradients. Figure 11(c) shows the valve in its fully open position and the local mesh refinement at work. We can see that the mesh is denser in the regions where the jet flow is developed and coarser in the regions where flow is fairly uniform. This helps us perform the flow computation efficiently.

Results are presented in the form of axial velocity contours and the von Mises stress distribution in Figure 12. The first panel shows the slice of axial velocity in frontal plane, the second panel shows the axial velocity contour extracted in the transverse plane near the commissural region. The third panel shows the von misses stress distribution on the leaflets. Figure 12(a) shows the valve configuration at 0.0125 seconds. At this time we can see a small jet forming at center of the valve as the orifice begins to expand. As leaflets start to deform and the belly starts bulging outwards, stress begins to build up on the leaflets in the belly region.

This is evident from the von Mises stress contour shown in figure 12(a). We can also observe that the stress is building up on the commissural regions as well mainly due to the expansion of the orifice. But note that the free edge is almost devoid of any stresses. As the velocity keeps increasing at the inlet, it was observed that the response of the leaflets to the pressure is instantaneous. At 0.031 seconds, we can observe from the figure 12(b) the leaflets have almost reached of fully its open configuration and the developed jet appears to be more centralized. From the axial flow contour we can also see a small negative velocity indicating flow reversal in sinus region although it was not prominent at this time. It was also observed that the deformation of the leaflets was not exactly identical although it was assumed that the geometry of the leaflets was identical at its initial configuration. At this time the stress was observed to be higher in the belly region, the commissures and also at the free edges of the leaflets. In our simulation the valve attains fully open position about 0.036 seconds which agrees with the physiological situation, i.e. between 30 and 40 millisecond [46, 25].

Figure 12(c) shows the valve configuration at 0.045 milliseconds. The valve has fully opened and formed a near circular orifice allowing a fully centralized flow. We can also see a strong jet that has developed. Owing to relatively different deformation process in each leaflet, we can observe that each the maximum stress magnitude is different in each leaflet. The maximum valve for each leaflet was around 60 KPa at the commissural region except for one leaflet which had maximum value of 90 KPa at one of its commissures.

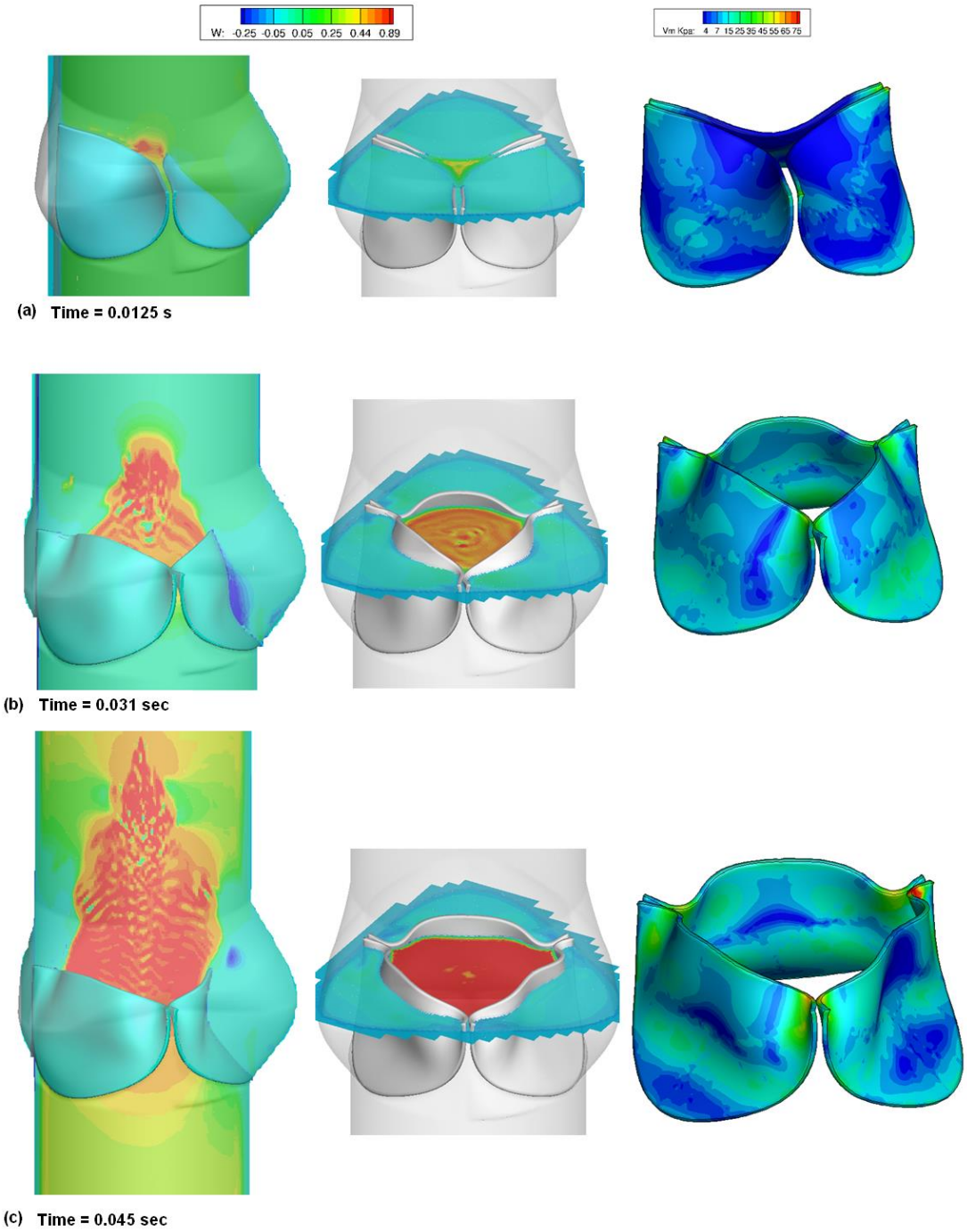

Figure 12: Axial velocity contour and von mises stress distribution during the various stages of valve opening. The curvature of the leaflets change during the opening phase and valve attains a fully open position around 35 millisecond which is similar to physiological situation (a) 0.0125 s (b) 0.031 sec (c) 0.045 sec

The simulation was allowed to continue until 100 milliseconds and it was observed that the leaflet deformation process was not identical with free edges of the leaflet especially during the later stages of opening. Once the valve attained its fully opened position, it started to vibrate. This could be due to the instabilities at the boundary layer emanating from the leaflet surfaces.

3.2 Discussion

The newly developed strongly coupled FSI presented in the previous sections is used to simulate the opening of a bioprosthetic valve. The main features of the model being a strongly coupled fluid structural interaction model where physiological flow rate was applied to simulate the opening behavior. Subiterations were performed in order to deal with the tightly coupled problem. Implementation of Aitken relaxation method enabled a faster convergence. The local mesh refinement algorithm was used to save computation time and also at the same time achieve adequate flow resolution. Figure 13(a) shows the behavior of the subiteration process for the entire simulation. On an average convergence was achieved approximately under 10 iterations although it took longer at the start of the simulation where the added mass effect dominates and also at the end of the simulation. This could be due to the instabilities from the jet. The flow solver was parallelized and 120 processors were used to partition the flow domain. This allows us to perform the simulation with a dense mesh which is absolutely necessary to capture the flow especially when at a physiological flow rate. The solid solution was performed using a single processor and information was broadcasted using MPI.

Figure 13(b) shows the amount of cells employed in this simulation. The simulation started with 800000 grid cells and as we marched in time, the local mesh refinement algorithm automatically adds more cells based on the flow gradients. Towards the end of the simulation, the maximum cells reached up to 1.3 million. It should be noted that a coarse mesh was used to simulate the problem and that explains the inadequate flow resolution obtained. Time dependent physiological flow rate was fed at the inflow plane and a Fung material model was used as a constitutive model to represent the leaflets with material constants obtained from experiments to obtain a physiological material behavior.

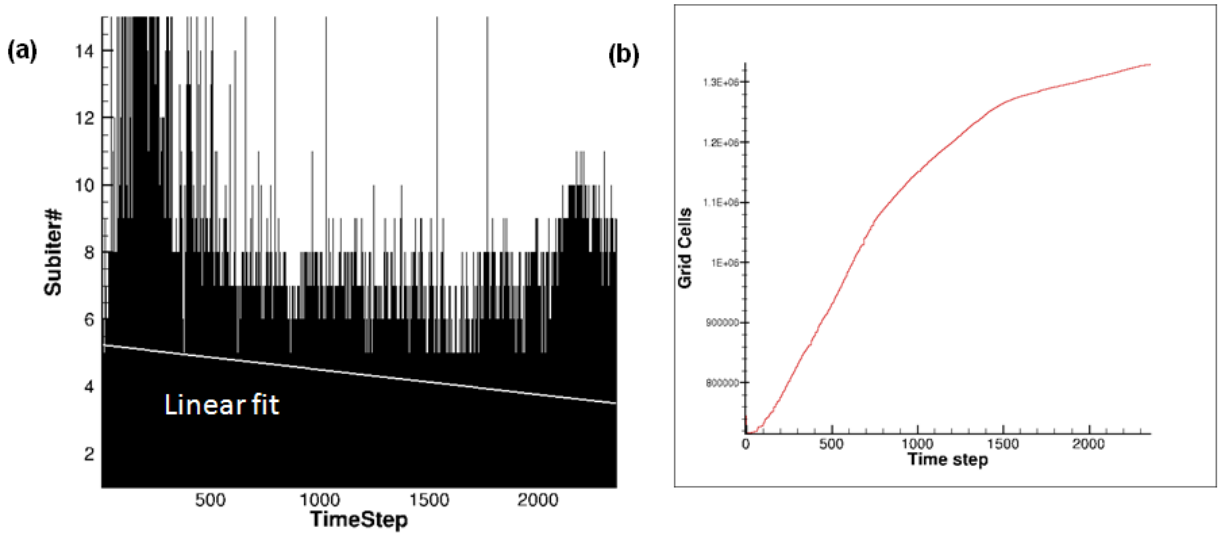

Figure 13: Subiterations are performed to deal with the instantaneous response of the leaflets to fluid force (a) Shows the subiteration number versus time step for the present study. (b) Shows the number of grid cells used for computation versus time

Past FSI studies on aortic valve such as de Hart et al used linear material model for leaflets. Use of a Fung material model is known to capture the behavior of leaflets better especially if experimental material constants are used [23]. Results showed that the leaflets response to the fluid load was almost instantaneous. The deformation started initially at the belly region of the leaflets with the curvature changing at the free edge. The three leaflets showed independent deformation and the valve attained a fully opened position around 36 milliseconds which is physiological as observed in various experiments [46]. Figure 14 shows the axial velocity profile at time 0.031 seconds and 0.045 seconds respectively. Assuming that the leaflet orifice is circular, the Reynolds number was computed to be 2100 and 3700 respectively.

Figure 15 shows comparison of leaflet deformation with some of the past studies conducted to understand the opening behavior of a bioprosthetic valve. Figure 15(a) and (b) shows the present results and Figure 15(c) are obtained from a flow visualization experiment of a bioprosthetic valve using a pulse duplicator. Figure 15(d) is deformation from a finite element study conducted by Kim et al [23]. Figure 15(e) shows the deformation of 2-D strongly coupled FSI study conducted at our lab. We can see that the deformation behavior obtained from the present study is in fairly good agreement with the other results presented.

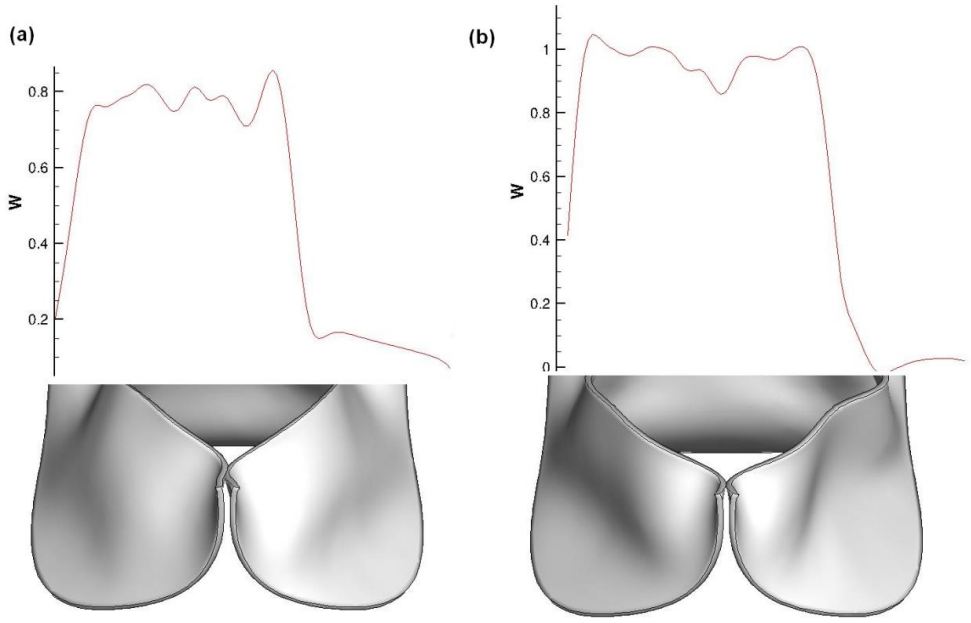

Figure 14: Axial velocity profile of the bioprosthetic valve at final stages of opening. (a) 0.031 sec (b) 0.045 sec

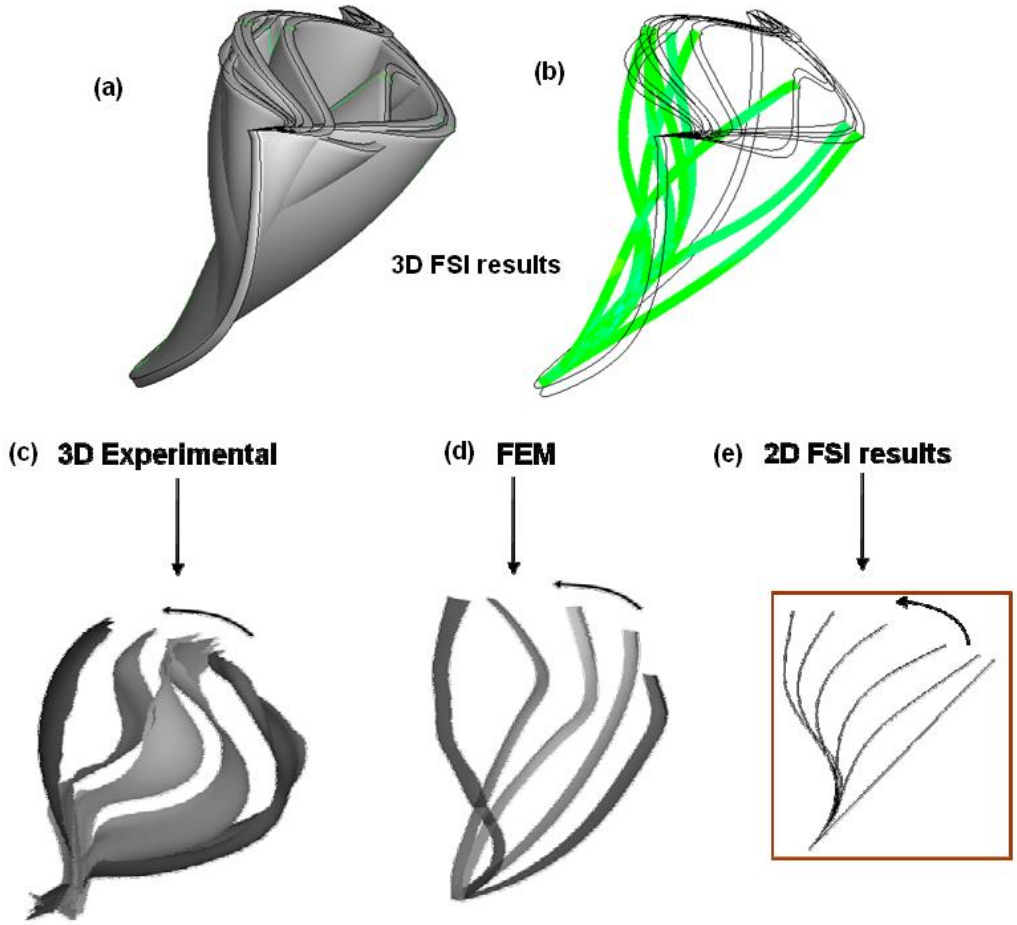

Figure 15: Comparison of present result with previous bioprosthetic valve studies: (a and b) shows the 3d valve deformation at various stages of valve opening and slices extracted at mid plane of the leaflet geometry. (c) Valve deformation obtained from 3D flow loop experiments. (d) 3D FEM computation (e) 2D FSI study

CHAPTER IV
FLUID STRUCTURAL INTERACTION OF BICUSPID AORTIC VALVE

Patients born with congenital bicuspid valves (BAV) may suffer from aortic stenosis or aortic incompetence and infective endocarditis. This condition where an individual is born with only two leaflets instead of the normal three cusps affects 1-2 % of population and is known to be one of the most common congenital anomaly [47, 48]. In addition, bicuspid valves are associated with other complications such as coarctation of aorta, aortic dissection and aortic aneurysm [49]. Study conducted by Larson and Edwards [50] emphasizes that the risk of aortic dissection is nine times greater in BAV. In addition to the above complications, with the older patients with BAV tend to have calcification and fibrosis which could affect the hemodynamics [51]. It is also suggested that the progression of calcification is more accelerated in the case of BAVs when compared to the normal tricuspid valves [52].

Studies conducted by Eisenberg et al., and Fedak et al., [53, 54] suggest that the cusp formation during valvulogenesis is directed by extracellular proteins and any abnormality in extracellular matrix may lead to abnormal cell differentiation and cusp formation during valvulogenesis. BAVs are usually characterized by unequal cusp size and there are different variants with or without a presence of a central raphe (a fibrous ridge) at the fusion site. Different anatomical variants of the BAV gives rise to different problems, for example, the fusion of the right coronary cusps and the non-coronary cusps is thought to have an increased risk of stenosis and incompetence as compared to other anatomical variants [49].

Finite element study conducted by [55] which compare the opening and closing behavior of different variants of BAV geometry showed that effective orifice

area during opening is significantly reduced in the case of BAV and the maximum in-plane von-mises stress on the leaflets is high compared to the normal leaflets particularly during the closing phase. Fluid structural Interaction study using BAV and TAV models conducted by Sucosy et al [56] showed that effective orifice area in BAV is reduced by 50% compared to TAV models. This study also revealed the existence of major differences in wall shear stress between TAV and BAV models. The group suggested that the elevated fluid shear stresses present in the BAV could trigger valvular inflammation. Although this study was able to characterize the flow and local wall stresses and compare the flow dynamics between the TAV and BAV geometries, the study was conducted in a two dimensional setting. Native aortic valve, both BAV and TAV are highly three dimensional in nature and a full three dimensional study is necessary to capture this effect. Moreover, the non-linear properties of the leaflets were not considered in this study. A multi-scale simulation of the BAV and TAV leaflets was conducted by Weinberg at al.[57] over different length scales as calcific aortic stenosis is thought to be a multi-scale process that spans from the cellular level to the organ level. The simulations are linked across the length scales to create the multi-scale model. It was reported that, at the cellular level, the deformation was not significantly different between the TAV and BAV even at the regions that are prone for calcification. At the organ level, it was observed that deformation of the bicuspid valve involved more flexure relative to the a normal aortic (tri-leaflet) valve and the effective orifice area is reduced at systole and the velocity profile showed a prominent jet formation with the BAV compared to a relatively flat centralized flow for the TAV.As the study did not observe any

substantial difference in deformation at the cellular level, the study concluded the genetic difference in both TAV and BAV in the extra cellular matrix constituents could play a major role in an accelerated calcification in BAV. However Mechanical deformations during the valvular dynamics cannot be undermined as a factor in early development or accelerated degenerative valvular diseases in patients with bicuspid aortic valves as they are exposed to high stress from a very early stage. In contrast stress overload on a normal aortic (tri-leaflet) valves develop only at later stages. The functional geometries of the TAV allow a full opening during systole and a wrinkle free closing behavior during diastole. In order to understand how a BAV functions, and why it fails Robicsek et al [58] used various techniques such as visual observations, silicon molds, intra vascular ultrasound, videography and digital modeling. Studies were performed using cryopreserved BAVs from humans in a left heart simulator. The valvular deformation and the fluid flow were recorded using 500 fps camera as well as ultrasound imaging techniques. Various parameters such as the shape of the orifice, aortic root functioning, valvular deformations were recorded. It was noted that the BAV had several compensatory mechanism such as folding or wrinkling in order to compensate for the unequal distribution of tissues. It was also noted that the flow was marked with turbulence and asymmetrical flow patterns due to the asymmetrical leaflets and the fully open configuration resulted in a elliptical shaped orifice. Stress analysis on the leaflets showed that there was uneven stress distribution in the two leaflets and one leaflet had relatively higher stress than the other which is seldom seen with the trileaflet valves. Altered flow in the ascending aorta due to the stenotic valve could result in a higher magnitude of

wall stress which could damage the endothelial lining in aorta. These changes in the wall could also play a role in causing dilatation and dissection [58].

The valvular deformation and the flow presented by a BAV can very well depend on its type and its functional geometry and hence could have a direct impact on the long term functionality of the valve. That is some BAV could function normally for a long time where as some others could fail in a few years. Fluid structural Interaction using patient specific geometries can be used as an efficient tool to understand the valvular deformation and flow patterns which would help us gain insight on the pathogenesis better and plan clinical steps accordingly. In the present work, patient specific bicuspid valve geometry is analyzed in the opening phase at a physiological Reynolds number using the FSI Algorithm developed. The valvular deformation process, the flow patterns are of particular interest.

4.1 Valve Geometry and simulation conditions

The bicuspid valve geometry was obtained from a male 19 year old patient using real time 3D (rt3D) ultrasound imaging. The image data is imported as point cloud format into the commercial meshing software GAMBIT. The point cloud date was connected using NURBS (Non Uniform Rational B splines) to obtain the leaflet and the aortic root geometry. Figure 16 shows the patient specific geometry used for the present analysis. The patient specific geometry data were obtained from Dr. Robert Gorman, M.D., Gorman Laboratories of the University Of Pennsylvania, College Of Medicine, Philadelphia for this collaborative study. The acquisitions of images from patients were performed following IRB approval and patient's informed consent. Figure 16(a) shows the view from the aorta and the sinus regions

are marked in the figure. The larger leaflet (L1), colored green is attached to the right coronary sinus and the non-coronary sinus. The smaller leaflet (L2) shown in blue is primarily attached to the left coronary sinus. It can be clearly observed from figure 16 (a) and (b) that the two leaflets are asymmetric. The two leaflet commissures are marked C1 and C2. C1 is the commissures at the junction of the left and the non-coronary sinus whereas C2 is between the right and the left coronary sinuses. The dimensions of the valve leaflet including the aortic root are given in table that accompanies with figure 16. It is assumed that the leaflets have a uniform thickness although in reality, the thickness of the cusps varies across its length. The aortic root and the leaflets are attached to an inlet and outlet conduit as shown in the figure. At the ventricular inlet, uniform time dependent axial velocity corresponding to a maximum flow rate of 450 ml/sec is applied as shown in the figure. The flow rate attained is approximately equal to the physiological flow rate attained during peak systole [25]. The aortic root and the sinus are defined as walls and do not take part in structural deformation in present work. All degrees of freedom are restricted along the edges where the leaflet is connected to the aortic root.

Once the valve reaches its complete opening in 30-40 milliseconds, the valve stays in its fully open configuration while the flow is still accelerating. As observed in the previous study, there is no appreciable deformation of the leaflets as far as the orifice area is concerned. At this time the fluid flow is still accelerating and this will go on until peak systole, hence fluid dynamics is of more interest at this stage. In order to save computational cost for this study and to focus on the flow dynamics,

the leaflets were held in its position once the valve attained its fully open configuration and the flow was allowed to accelerate according to the inflow conditions.

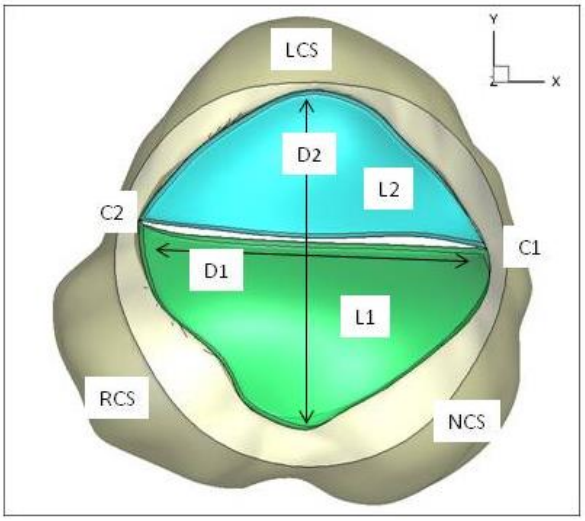

D	D1	D2	H	t
2.4	3.34	2.7	8.35	0.06

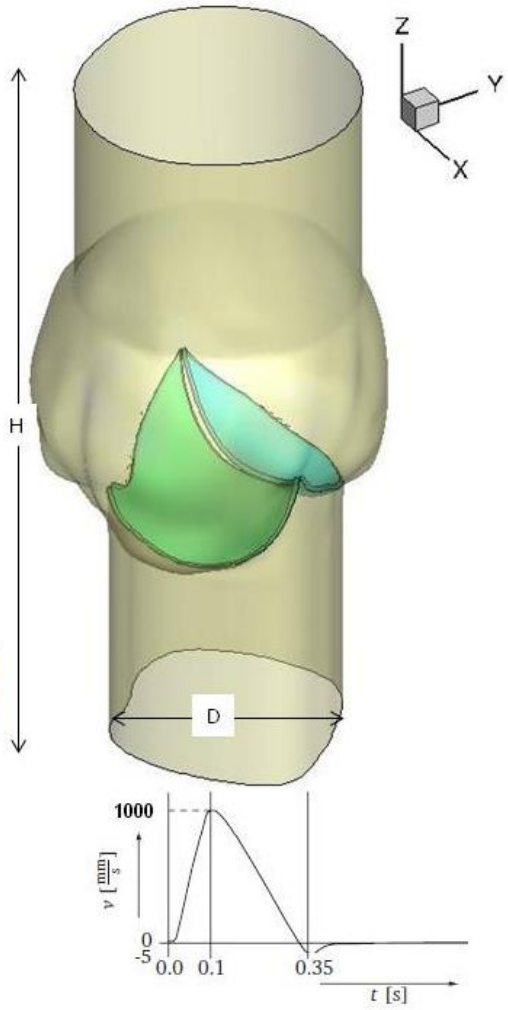

Figure 16: The bicuspid aortic valve geometry with dimensions. (a) View from the aortic side. LCS, RCS and NCS are left, right and non-coronary sinuses respectively. (b) Shows the computational domain with the leaflet and the aortic sinuses and the applied boundary conditions. Simulation is continued until 100 milliseconds. All dimensions are in cms.

4.2 Results

Results of this simulation is presented as two sections, the first one will show the results until the valve reaches complete opening and the second section will focus on the fluid dynamics of the valve during peak systole when the valve has reached its fully open position and stays open while the flow is still accelerating.

Valve opening: During the initial stages of the valve opening, the leaflets undergo rapid deformation to accelerating flow until it reaches its opening position. Hence during the initial stages, both the solid and the fluid dynamics are important. Various stages of valve opening are shown in figure 17. The first panel shows slices of the axial velocity contour. The slices are extracted at the mid- plane of valve. The second panel again shows the axial velocity from the aortic view through a slice extracted at the Z plane just above the valve commissures. The third panel shows the von-mises stress distribution on the leaflet. Owing to the asymmetry of the two leaflets, it can be anticipated that the leaflet deformation are going to be different from each other and flow pattern different relative to a tri-leaflet valve. From the initial configuration shown in the figure 16 (a) and also from Figure 17(a) we see that the two leaflets together form a slit like opening at the free edge. As the velocity increases at the inlet, pressure build up on the ventricular side of the valve begins to push the valve open. Assuming that the fluid to solid response time scale for a bicuspid valve will be approximately equal to that of a bioprosthetic valve, the deformation of the solid can be anticipated to be instantaneous in this case as well. Although the magnitudes of the pressure is higher on the belley we donot see an appreciable deformation of the belly at the initial stages of the valve. This could be

because of the lack of surface area near the belly reagion to allow sufficient deformation to take place. Figure 17(b) shows the valve configuration at 0.01 sec. We can observe that , instead of the orifice area expanding from the center as we saw in the bioprosthetic valve, the leaflets open from the region closer to commisure 1. In a normal tri leaflet valve and also in bioprosthetic valves, it has been observed the the expansion of orifice starts from the center of the valve thus allowing a central flow in the fully open position. In the present case, the expansion of the orifice was observed to be offcenter even in the initial stages for both the leaflets. This behaviour seems to continue for the rest of the deformation process. At time = 0.016 sec we can observe that the valve orifice has expanded more near the commisure C1 than compared to C2. Meanwhile as the valve starts opening a jet begins to develop as the valve starts to open. Because of the slit like opening formation presented by the valve, we can observe that the magnitude of flow is greater near the slit or the commissures than at the center. This is clear from the second panels of figure 17 showing the axial velocity from a slice extracted from the Z plane. As the valve begins to open further, we begin to observe that the magnitude of velocity near fibrosa is low indicating a development of negative velocity although we do not observe any recirculation at this time. At time 0.025 sec, the valve has almost reached its fully opened position as indicated in figure17 (f). we see that the jet has developed more and appears to me asymmetric. We also see that the a weak vortical structure begins to form on the aortic side (fibrosa) of the leaflet in the sinus region. Figure 17 (e) shows the opening stage at 0.033 sec where the valve seems to have attained its fully open configuration. There seems to be no

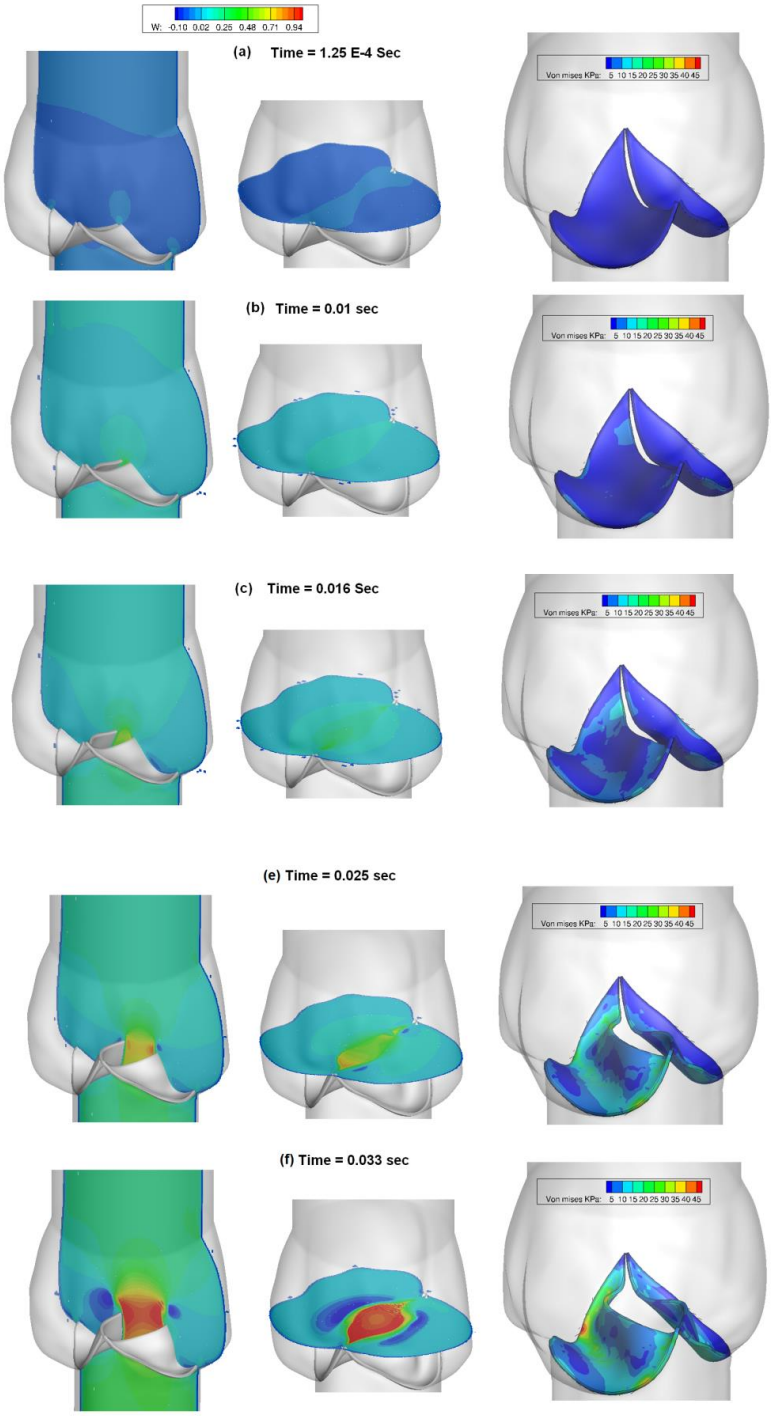

Figure 17: First two panels shows the axial velocity contours and the third panel shows the von mises stress distribution at various stages of valve opening. Flow results show that the developed jet is off centered and near the commissural region and the deformation of the valve also appears to be asymmetrical resulting in an ellipsoidal shaped orifice.

Post opening: Figure 18 shows the results of the valve fluid dynamics during the later part of the systole. The first panel shows the axial velocity contours with slices extracted in the X and Y plane from which we can see the axial jet. The second panel shows the vorticity countour at their respective times.

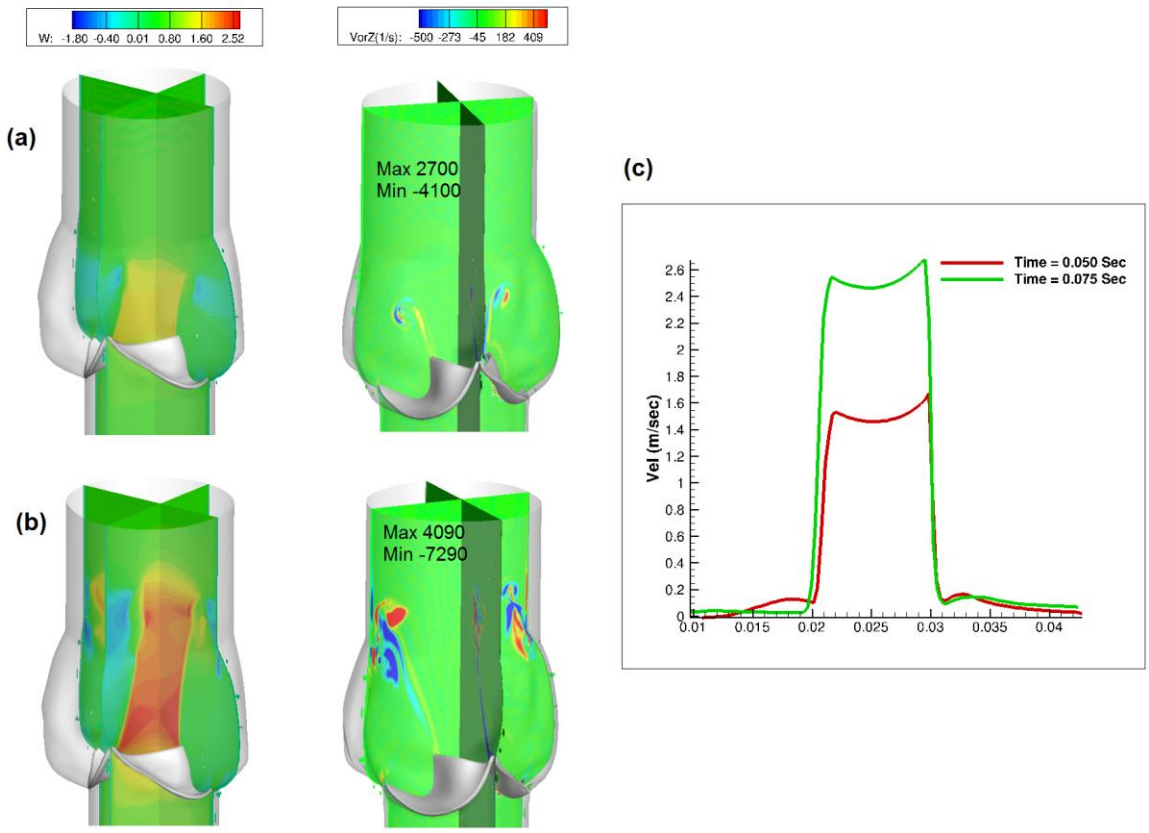

Figure 18: The axial velocity contours and the Vorticity contours at time (a) 0.050 sec (b) 0.075 seconds (c) shows the corresponding axial velocity profiles. The axial velocity contours and the vorticity contours during peak systole shows strong jet development, vortical structures and recirculation zones near the sino-tubular junction

appreciable change in orifice region between the valve configuration at 0.025 ms and 0.033 sec indicating that the valve has attained its full open position. The velocity magnitude of the jet was approximately 0.9 m/sec and the corresponding Reynolds number reads 2500. We can easily observe that the valve in its fully open configuration is stenosed . The jet at the center of the valve seems to have gained strength now and the recirculation region in the sinus has also grown stronger and is starting to dominate the sinus region.

Figure 18(a) shows the axial velocity and vorticity contours at 0.050 seconds, i.e. approximately 0.012 seconds after the valve has reached its fully open position. As it was observed earlier that the valve leaflet appeared to be stenosed, we can anticipate that the jet will be stronger in this case than compared to a trileaflet valve which will have a larger and a circular orifice area. The jet seems to have grown stronger owing to the accelerating flow and the reduced orifice area as the maximum velocity magnitude reached approximately 1.5 m/sec at 0.050 seconds with a corresponding Reynolds number of 3900. From the vorticity contours we can also observe that the boundary layer at the valve edge has thickened and has started to separate from the free edges of the leaflet. We can also see that a recirculating flow has developed in the sinus region of the valve. Figure 18 (b) shows the flow results at 0.075 sec, we see that the jet has grown much stronger with a velocity magnitude of approximately 2.5 m/sec and the Reynolds number was computed to be 6900. Here we can observe a strong interaction of the opposite signed vortices which had developed from the free edges of the leaflet and from the sinus walls in the sino-tubular junction indicating a strong recirculation region.

4.3 Discussion

The present highly resolved calculations based on cartesian mesh with the employment of local refinement algorithm enabled us to capture the significant flow dynamics during the opening stages of a patient specific bicuspid valve model. The strongly coupled FSI algorithm and the use of LMR enabled us to capture the valve deformation process at a physiological flow rate. Figure 19 (a) and (b) shows the cells dynamically recruited for the flow computations using LMR. The number of cells at the start of the simulation was around 4 million and as the flow rate increases, the dynamics becomes more complex and LMR dynamically refined the mesh to achieve a good flow resolution. At the end of the simulation (using 256 processors) we can see that the total cells in the flow domain reaches close to 10 million grid points. Figure 19(c) shows the number of subiteration requited per time step. On an average, the number of subiteration required was 8 although the number was high during the initial and the final stages of opening . Highly resolved flow computations on patahological models such as BAV would help us gain insight into the flow dynamics and its implications due to the malformed geometries.

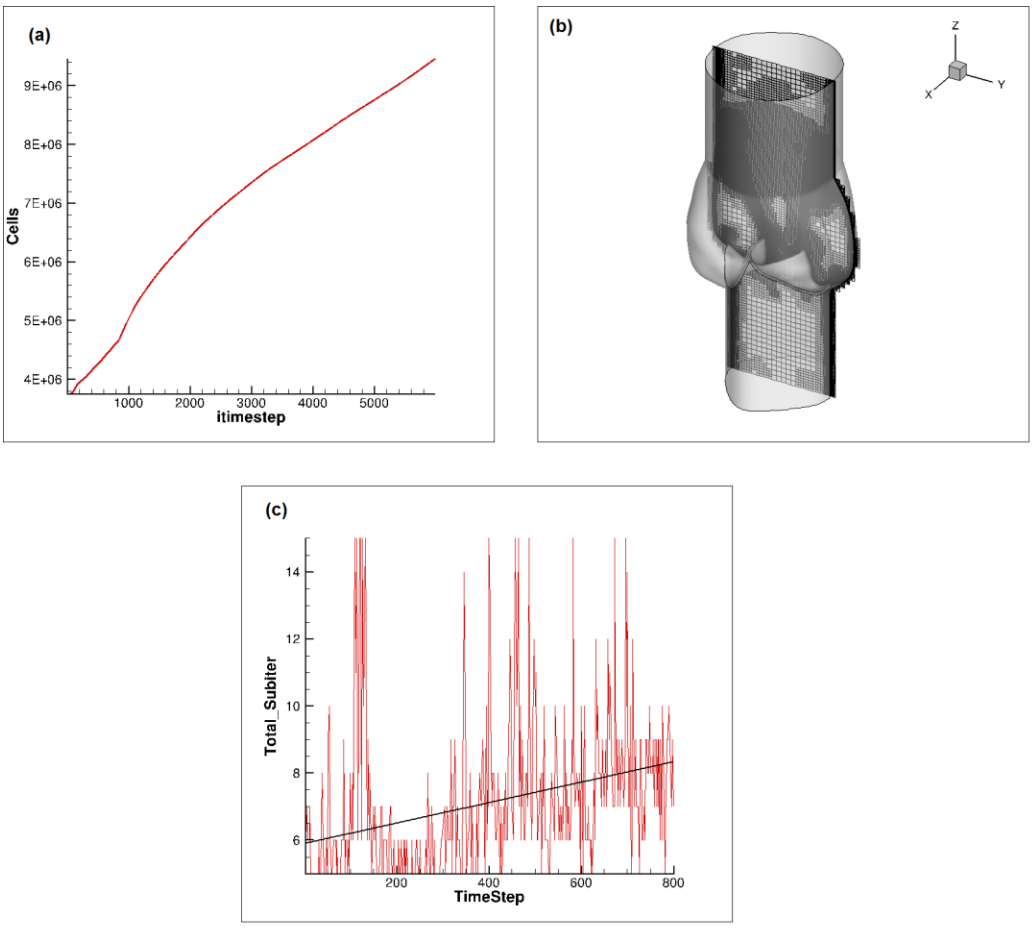

Figure 19: A high density mesh was used to capture the flow at a physiological Reynolds number. Use of LMR enabled efficient computing. The simulation started with 3 million grid cells and as the increased with the flow and finally reached 10 million grid points which enabled adequate flow resolution. (a) The number of cells recruited for the computation (b) subiteration versus time. (c) Shows the Cartesian mesh with LMR in action

From the results presented in the previous section, we could observe that the shape of the final orifice was roughly elliptical instead of a circular orice normally observed in a trileaflet valve. The same type of deformation and a final elliptical orifice was also observed by Robicsek et al [58] from a pulse duplicator experiment and also by Conti et al in their image derived FE model [68].

In a healthy trileaflet valve, blood flow accelerates and reaches around 1.35 m/sec during peak systole [Chapter 7 [8]]. In the present simulation, we observe that during the peak systole the velocity magnitude reaches around 2.5 m/sec mainly due to the reduced orifice area. This could have profound effects on the fluid shear stress. The high velocity jet could impinge on the walls of the aorta and damage the endothelial linings. These changes in the wall could also play a role in causing dilatation and dissection [58]. During peak systole we also saw boundary layer separation from the leaflet edges and interaction of vortical structures. The interaction between the separated boundary layer from the leaflet edges and the weak flow in the sinus region together present a complex flow dynamics in the sino-tubular junction. This could impact the flow dynamics in the ascending aorta as well.

CHAPTER V
FLUID STRUCTURAL INTERACTION OF NORMAL (TRI-LEAFLET) AORTIC VALVE

In this section, we examine the fluid dynamics and the solid deformation associated with the opening of a normal aortic valve. A healthy aortic valve comprises of three semilunar cusps or leaflet attached to the fibrous ring which in turn are attached to the fibers of the ventricular septum and the anterior leaflet of the mitral valve. The sinus of the Valsalva or the aortic sinus is situated superior to this ring. The aortic sinus mainly consists of three bulges which align with the belly of the leaflet. The right and the left coronary artery which supplies blood to the heart arises from the right and left sinus and hence named as right and left coronary sinuses. The third sinus is called the non-coronary sinus.

Using real time 3D (rt3D) ultrasound imaging, the trileaflet aortic valve geometry was obtained from a male 56 year old patient with atrial fibrillation. The image data is imported as point cloud format into the commercial meshing software GAMBIT. The point cloud date was connected using NURBS (Non Uniform Rational B splines) to obtain the leaflet and the aortic root geometry. The trileaflet geometry data was also obtained from Dr. Robert Gorman, M.D., Gorman Laboratories of the University Of Pennsylvania, College Of Medicine, Philadelphia for this collaborative study. The acquisitions of images from patients were performed following IRB approval and patient's informed consent. Figure 20 shows the geometry of a tri-cusped valve in its closed configuration. The geometry was obtained using the same method as briefed in the BAV study. Figure 20(a) shows the front view of the valve and the second panel shows the top view of the aortic valve. The left, right and the

noncoronary leaflets are marked. We can see that that the noncoronary cusp appears to be the largest and the other two leaflets are approximately the same size. During the opening phase of the valve, the semilunar cusps open by changing its curvature at the free edge in response to the pressure applied as the result of ventricular contraction during systole. In order to simulate the opening of the leaflets, uniform time dependent axial velocity corresponding to a maximum flow rate of 450 ml/sec is applied. The applied flow rate is approximately equal to the physiological flow rate attained during peak systole [25]. As shown in the figure, the aortic root is extended downwards to depict the ventricular inlet and similarly a conduit is attached to the sinutubular junction to represent the ascending aorta. The aortic root and the sinus are defined as walls and do not take part in structural deformation in this analysis although in reality, this is not the case. The opening phase of the leaflet consists of interplay between the roots and the leaflet in which the action of the root helps the valve to open much more efficiently. It has been shown that the expansion of the root helps in almost 20% of the valve opening [22].

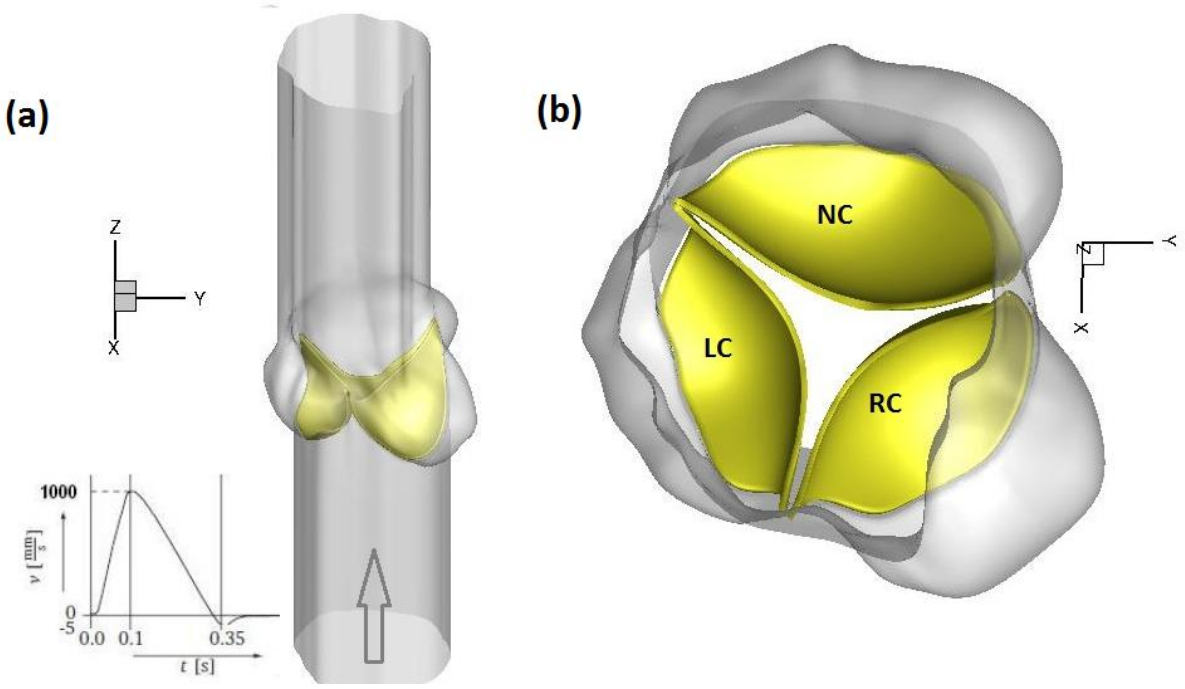

Figure 20: The normal aortic (tri-leaflet) aortic valve geometry. (a) Shows the computational domain with the leaflet and the aortic sinuses and the applied boundary conditions. (b) View from the aortic side. LC, RC and NC are left, right and noncoronary leaflets respectively.

5.1 Results

The results of the present simulation are presented in figures 21 and 22. The first panel shows the slice of axial velocity cut from the X and Y plane approximately at the mid-section of the valve geometry, the second panel shows the axial velocity contour extracted in the transverse plane near the commissural region. The third panel shows the root mean square of the displacement of leaflets at various stages of opening. Pressure build up on the ventricular side of the leaflet during early systole causes the valve to respond to the force passively. It was observed in the bioprosthetic valve simulation that the earlier staged of valve opening was almost

symmetrical although in the later stages, the leaflet deformation process was asymmetrical. In contrast, a normal aortic (tri-leaflet) leaflets had an asymmetrical pattern right from the beginning of simulation. This could be largely due to the geometry of the leaflets. It was also observed that the individual deformation pattern of the left and right coronary leaflets showed signs of asymmetry with in itself if a plane was cut at the midsection of the respective leaflets. The noncoronary leaflet had almost a symmetrical pattern of deformation relative to the other two. This trend can be observed from the contours of displacement in figures 21 (c) and (d). The time at this point is 0.025 and 0.04 ms into the simulation. The deformation pattern appears to be asymmetrical and highly three dimensional, yet the collective deformation of the leaflets result in the formation of a circular orifice which begins to expand from the center. This is apparent from the jet flow that starts to develop at the center which can be observed from figures 21 (c) and (d). From figure 21(d) we can also observe that the valve has nearly reached its fully open position. Figure 22 (a) shows the simulation results at 50 milliseconds. We can clearly see that the valve has reached its fully open position and a central jet has developed with a nearly circular orifice. Once the valve has reached its fully open position, the free edges of the leaflets keep deforming owing to the accelerating flow during peak systole although maintaining a circular orifice throughout the entire simulation as observed in 22 (b), (c) and (d). It should be noted that the present simulation was carried out with a coarse mesh and this resulted in a low resolution of flow particularly during peak systole. The velocity attained at 70 milliseconds was measured to be approximately 1.5 m/sec as shown in figure 23. It has

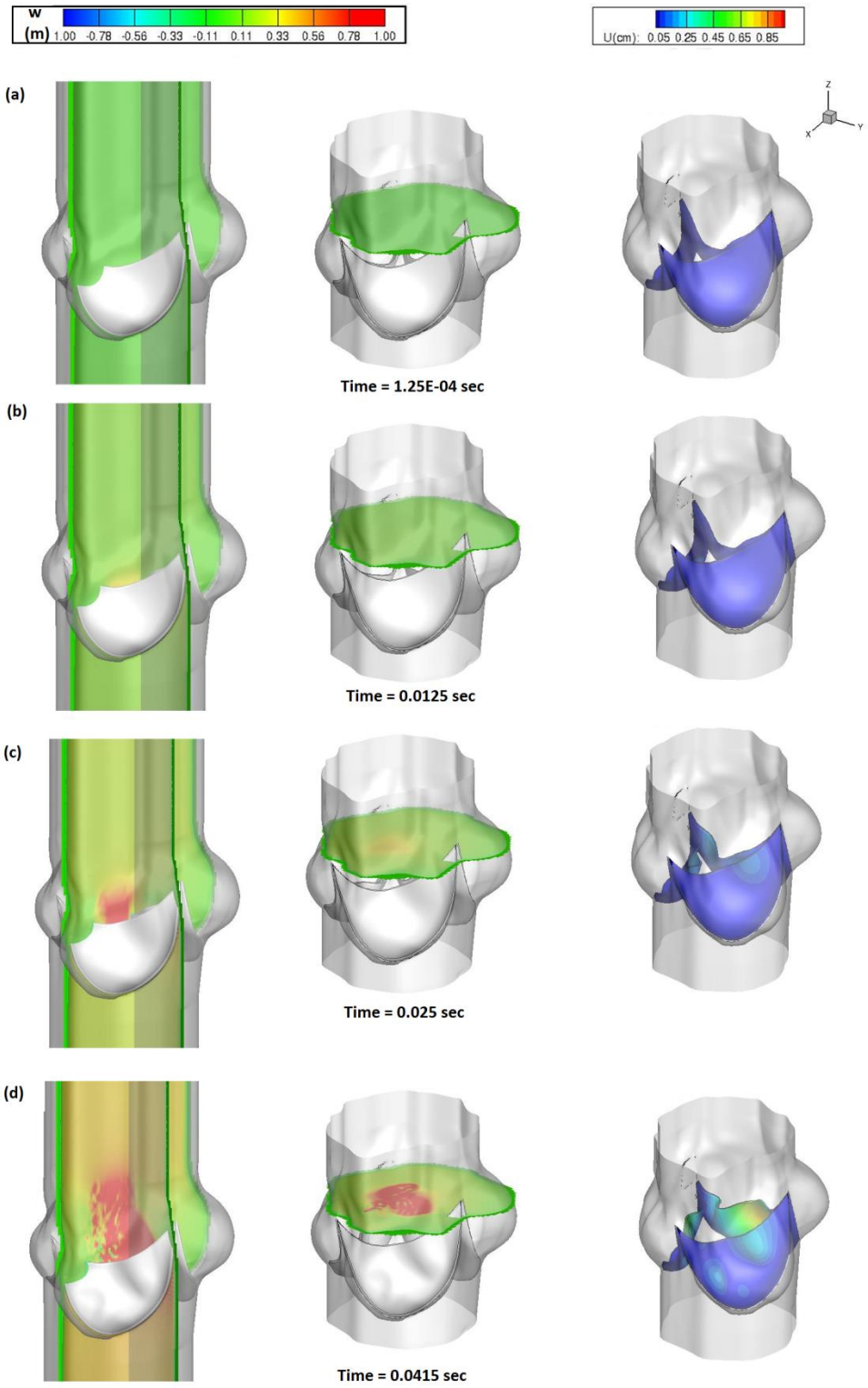

Figure 21: The axial velocity contour and root mean square of displacement at initial stages of valve opening (a) 1.25e-04 s (b) 0.0125 sec (c) 0.025 sec (d) 0.0415 sec

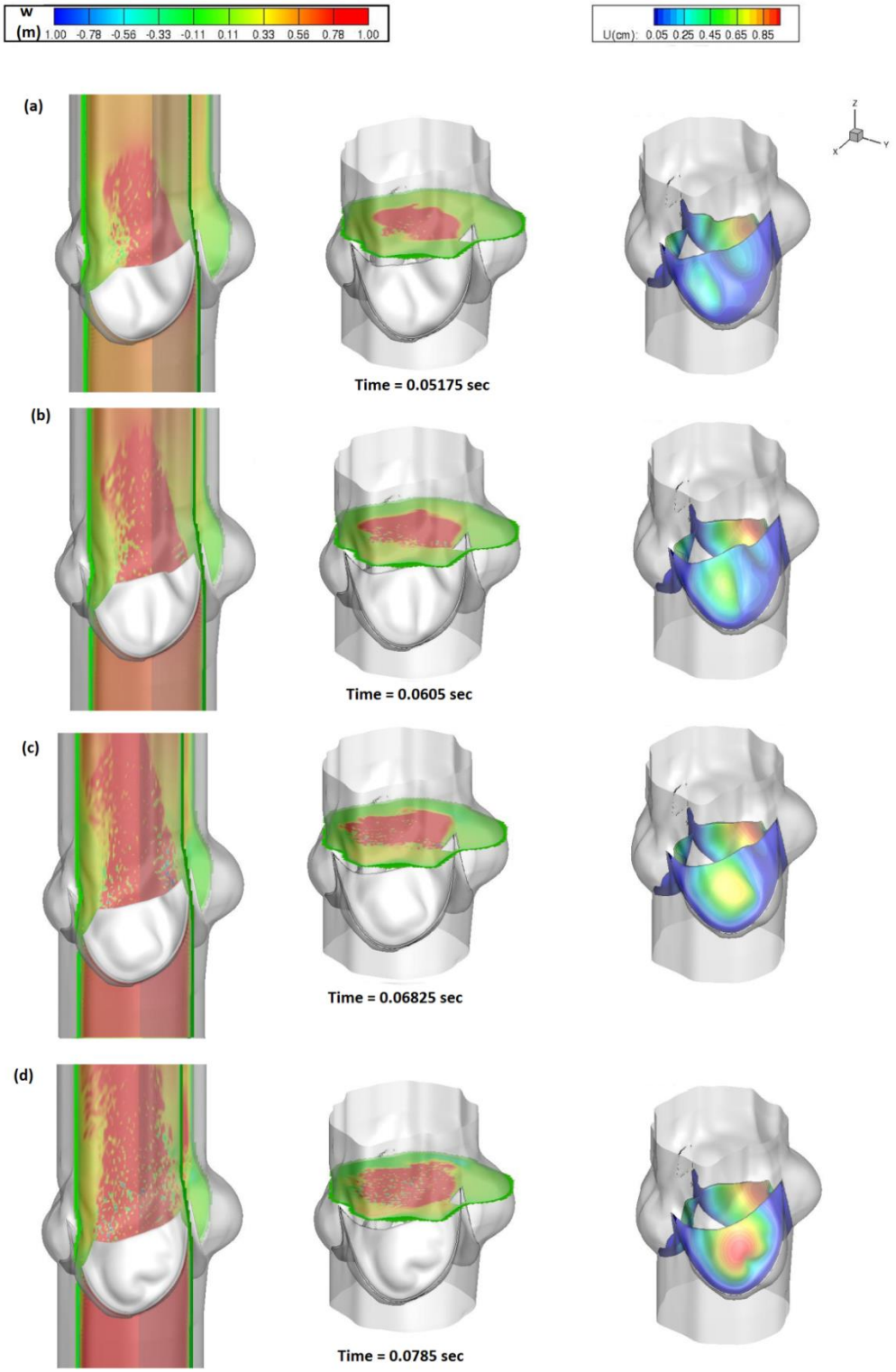

Figure 22: The axial velocity contour and root mean square of displacement at final stages of valve opening (a) 0.051 s (b) 0.06 sec (c) 0.068 sec (d) 0.078 sec.

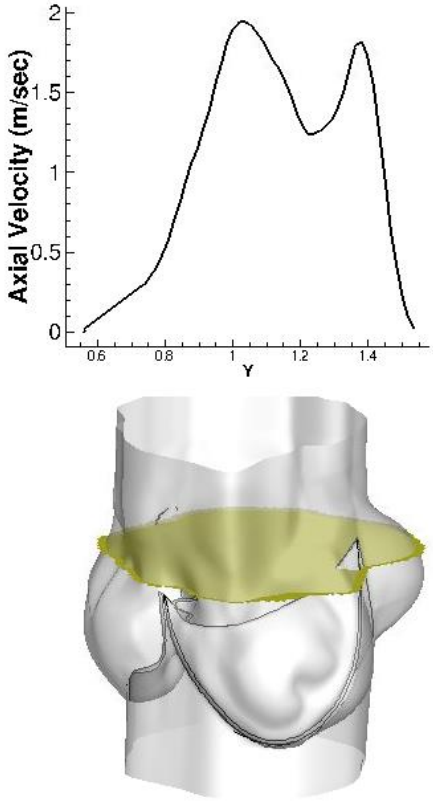

Figure 23: The axial velocity profile of the a normal aortic (tri-leaflet) aortic valve during peak systole. The velocity was measured at the sinutubular plane as marked in yellow. Axial velocity profile shows a skewed pattern with a mean velocity around 1.5 m/sec.

been observed that in healthy individuals, the velocity during systole reaches a peak value of 1.35 ±0.35 m/sec. Although the computed velocity is fairly close, more accurate flow computation needs a highly resolved flow particularly to capture the recirculation in the sinus region.

CHAPTER VI
SUMMARY, LIMITATIONS AND FUTURE STUDIES

The strongly coupled 3-D FSI algorithm developed in the current work has been utilized to simulate the opening phase of a bioprosthetic valve model and a patient specific bicuspid aortic valve. The FSI algorithm was developed using a partitioned approach using two independent solvers for the flow and the solid domain. The flow solver employed is ELAFINT 3D which has been fully parallelized so that the domain can partitioned and the computation distributed among various processors. Thus enabling us to complete the simulation in a fraction of time than required by a single machine. The fully parallelized flow solver equipped with a local mesh refinement algorithm which dynamically refines mesh based on flow gradients enabled us to perform the simulation at a physiological flow rate maintaining a good level of accuracy meanwhile saving computational time. All the simulations used the University of Iowa 's HELIUM Cluster. A FEAP based solid solver was used to capture the solid deformation. Enhanced assumed solid shell element routine (developed by Vu- Quoc et al) which has the ability to provide a good coarse mesh accuracy was incorporated to the solid solver and Newmark algorithm was used to obtain the velocity and the acceleration. Because only a single layer of element is sufficient for the EAS element to capture an accurate deformation, the same surface mesh which are used to generate the levelset can be used as the lagrangian mesh for solving the structual deformation as well. In other words, The surface mesh for levelsets which is defined by a 4 node quadrelateral elements and the 8 node solid shell elements for the structure solution will use the same nodes, just a different connectivity list. Implementation of an experimentally

derived Fung model enables us to capture the realistic deformation process. Previous FSI Studies conducted on aortic valves included linear material to represent the valve material, reduced flow rate becase of a low density fluid mesh which resulted in a late valve opening [25]. Simulations of the valve opening using the present algorithm showed that the valve attains full opening in around 30 millisecond identical to the physiological situation. The FSI algorithm used in this study is based on a strongly coupled partition approach which was implemented in a 2-D setting developed previously in our lab [26]. With that algorithm, we were able to analyse the opening dynamics in a 2-D setting with physiological inflow conditions. The present work can be viewed as a direct extension which adds 3-D FSI capability for simulating tissue valve problems. Kunzelman et al.,[69] used a full three dimensional FSI analysis to simulate a mitral valve function to study the roles of individual components of mitral valve and to evaluate surgical valve repair techniques. Parameters of the material model were varied to simulate patological conditions. An exprimentally driven microstructural material model was used to represent the mitral valve leaflets. A staggered approach was used and information from the fluid and solid were exchanged once per time step thus making this a weakly coupled approach. Small time step size were used to minimize errors. This approach might not be ideal especially with very thin leaflets such the bioprosthetic valves and aortic valves which increases effect of added mass to the coupling [42,44,64,65]. Present FSI algorithm deal with this effect through the means of subiterations which stabilizes the system with in the time step. Aitken relaxation is

used to dynamically speed up the the convergence. This allows us to use larger time step size for our simulations.

6.1 Validation

The validation of the algorithm was done using a test case proposed by Neumann et al. [66] and also studied by Idelsohn et al. for testing a Monolithic FSI algorithm [60]. Results from the present FSI algorithm which used a St. Venant Kirchhoff material for constitutive modeling of the flap showed a good overall agreement in the behavior of the flap such as similar tip deflection, retraction of the plate after the maximum velocity was reached and an eventual steady state, but the recoil magnitude was different. Hence further investigation; especially in the solid sub domain concerning the material model is necessary to draw out the difference. The difference in material behavior especially in the later stages could be due to the different material model used in both studies. We do not know what material model was used by Idelsohn et al [60] to represent the material and how the structural solution was obtained for example, the structural model could have been a small displacement model or a large displacement model. So the elastic modulus, E used in that study may not be suitable in our case where the element routine is non-linear and more suitable for large displacement problems, the St. Venant Kirchhoff material model also falls into the non-linear regime. These could have made the flap behave stiffer during the later stages of simulation as we observed in results presented in the validation section. In order to find that, a structural analysis of the flap with the material properties used by Idelsohn et al [60] is under way using the commercial software Ansys. The deformation behavior is recorded and compared

with the deformation obtained by the newly developed FEAP based solver with the EAS solid shell element and Kirchhoff model. With trial and error, an E′ can be obtained which would be identical to the deformation obtained from the original model. This E' can be used for the purpose of validation to see if an identical behavior of the flap can be established throughout the entire simulation.

6.2 Limitations

Although the present strongly coupled FSI framework was able to simulate the opening dynamics of aortic valves, there are several limitations which will be outlined in the following section. Firstly, all the simulations performed on the aortic valves assumed the aortic root to be rigid and the root did not take part in the deformation process. It has been observed that the opening phase of the valve involves the action of root which aids in an efficient opening of the valve. The dynamics of the root are also a result of the roots passive response to the pressure gradient. Gnaneshwar at el [22] observed that the aortic root starts to expand early in the opening phase and aids in almost 20 % of the valve opening. This dynamics of the root could help the valve to open much faster. In the present thesis, we note in the normal aortic (tri-leaflet) valve simulation that, the valve attains its fully open position between 40 and 50 milliseconds. In vivo measurements of aortic valve orifice area using real time measurement system on dogs showed that the duration of aortic valve opening lasts only 36.2 ± 8 milliseconds [72]. Inclusion of the root in the simulation could shed light in the difference observed. Future simulation will include the root geometry in order to gain a better understanding of the opening dynamics of the aortic valve.

Vigmostad et al [26] implemented an implicit scheme to incorporate the Neumann boundary condition. This interface treatment incorporated the solid acceleration into the discreet pressure Poisson equation. The inclusion of solid acceleration into the boundary condition will capture the full effect of the added mass effect which is inherent in FSI systems such as tissue heart valves. The implicit scheme incorporated by Vigmostad et al enabled a faster convergence of the pressure Poisson equation. Efforts are underway to implement this implicit approach in the current 3-D framework. As indicated earlier, the interface is represented by levelsets which are signed distance functions. The levelsets are generated using an input surface mesh for the first time and subsequently generated using the information supplied by the solid solver. In the current framework, while subiterations are performed with in the time step to deal with the instabilities, the levelsets are generated only once per time step as within the time step, displacement is assumed to be very small. This forces us to use small time step size. In order to use sufficiently larger timesteps that will allow larger displacements to take place, levelsets should be generated within the Subiterative procedures. Efforts are underway to include this as well.

Present solid solver does not have the contact algorithm which is essential for simulating the closing mechanism a tissue valve. The leaflets would coapt during closure and this very important and an essential process cannot be captured without a contact algorithm in the solid solver. Efforts are underway in developing a NURBS based solid solver with contact algorithm which when coupled along with

the parallelized flow solver would enable us to perform simulations of an entire cardiac cycle using physiological conditions and material properties.

REFERENCES

[1]. Bodnar, E., Grunkemeier, G. L and Gabbay, S, *"Heartvalve replacement: A statistical review of 35 years' results – Discussion.*, 1999,The Journal of Heart Valve, Dis. 8, p. 470–471.

[2]. Butchart, E. G., et.al. *"A new scoring system to determine thromboembolic risk after heart valve replacement",* 2003, Circulation, v. 108, p. 68–74.

[3]. Giddens, D. P., Yoganathan, A. P and F. J. Schoen, *"Prosthetic cardiac valve,* 1993, Cardiovascular Pathology, v. 2, p. 167–177.

[4]. Hammermeister., K, E, et.al. *"A Comparison of Outcomes in Men 11 Years after Heart-Valve Replacement with a Mechanical Valve or Bioprosthesis".* 1993, NEJM, v. 328, p. 1289-1296.

[5]. Sachweh, J. S and Daebritz, S.H, *"Novel "biomechanical" polymeric valve prostheses with special design for aortic and mitral position: a future option for pediatric patients?"*, 2006, ASAIO, v. 52(5), p. 575-80.

[6]. Vesely, I, *"The evolution of bioprosthetic heart valve design and its impact on durability",* 2003, Cardiovascular Pathology, v. 12, p. 277- 86.

[7]. Thubrikar, M. J, et.al. *"Role of mechanical stress in calcification of aortic bioprosthetic valves,* 1983, Thoracic and Cardiovascular Surgery, v. 86, p.115–125.

[8]. Chandran, K. B., Stanley E. Rittgers and Yoganathan, A. P, *"Biofluid mechanics: the human circulation"*. 2007, v. 7, p. 257.

[9]. Gallegos, R. P and R. Morton Bolman III, *"Handbook of cardiac anatomy, physiology and devices",* 2009, Humana Press Inc. p. 385-403.

[10]. Krishnan, S, *"Two-Dimensional Dynamic Simulation of Platelet Activation During Mechanical Heart Valve Closure",* 2006, Annals of Biomedical Engineering, v. 34, p. 1519-1534.

[11]. Govindarajan, V., Udaykumar H. S and Chandran K. B, *"Two-Dimensional Simulation of Flow and Platelet Dynamics in the Hinge Region of a Mechanical Heart Valve".* 2009, Journal of Biomechanical Engineering, 131(3): 031002.

[12]. Govindarajan, V, et.al. *"Two-Dimensional FSI Simulation of Closing Dynamics of a Tilting Disk Mechanical Heart Valve"*, 2010, Journal of Medical Devices, v. 4(1): 11001.

[13]. Govindarajan, V, et.al. *"Impact of Design Parameters on Bi-leaflet Mechanical Heart Valve Flow Dynamics".* 2009, Journal of Heart Valve Disease, v. 18, p. 535–545.

[14]. Govindarajan, V., Udaykumar, H. S and Chandran, K. B, "*Flow dynamic comparison between recessed hinge and open pivot bi-leaflet heart valve designs".* 2009, Journal of Mechanics in Medicine and Biology, v. 9(2), p. 161–176.

[15]. Schoen, F. J., Levy, R. J., *"Tissue heart valves: Current challenges and future research perspectives"*, 1999, Journal of Biomedical Materials Research, v. 47, p. 439–465.

[16]. Thubrikar, M. J, et.al. *"Role of mechanical stress in calcification of aortic bioprosthetic valves"*, 1983, Journal of Thorac Cardiovascular Surgery, v. 86, p.115-125.

[17]. Thubrikar, M. J., Aouad, J and Nolan, S. P, *"Patterns of calcific deposits in operatively excised stenotic or purely regurgitant aortic valves and their relation to mechanical stress"*, 1986, The American Journal of Cardiology, v. 58, p. 304-308.

[18]. Schoen, F. J, *"Cardiac valve prostheses: review of clinical status and contemporary biomaterials issues",* 1987, Journal of Biomedical Materials Research, v. 21, p. 91– 117.

[19]. Levy, R. J., Schoen, F. J and Golomb, G, *"Bioprosthetic heart valve calcification: clinical features, pathobiology and prospects for prevention,* 1986, CRC Critical Reviews in Biocompatibility, v.2, p. 147– 87.

[20]. Vyavahare, N, et.al. "Mechanisms of bioprosthetic heart valve failure: Fatigue causes collagen denaturation and glycosaminoglycan loss", 1999, Journal of Biomedical Materials Research, v. 46, p. 1097-4636.

[21]. Yoganathan, A. P., He, Z and Jones, S. C., "Fluid mechanics of heart valves" 2004, Annual Review of Biomedical Engineering, v. 6, p. 331 -362.

[22]. Ramakrishna, G., Kumar, R. K and Balakrishnan, K. R**.** *"Dynamic analysis of the aortic valve using a finite element model",* 2002, The Annals of Thoracic Surgery, v. 73, p. 1122-1129.

[23]. Kim, H, *"Dynamic Simulation of Bioprosthetic Heart Valves Using a Stress Resultant Shell Model",* 2008, Annals of Biomedical Engineering, v. 36, p. 262-275.

[24]. Hart, J. D, et.al*, "A two-dimensional fluid-structure interaction model of the aortic valve"* 2000, Journal of Biomechanics, v. 33, p. 1079-88.

[25]. Hart, J. D, et.al, "A three-dimensional computational analysis of fluid–structure interaction in the aortic valve", 2003, Journal of Biomechanics, v. 36, p. 103-112.

[26]. Vigmostad, S. C, et.al. *"Fluid–structure interaction methods in biological flows with special emphasis on heart valve dynamics",* 2010, International Journal for Numerical Methods in Biomedical Engineering, v.26, p. 435–470.

[27]. Ye, T, et.al. *"An Accurate Cartesian Grid Method for Viscous Incompressible Flows with Complex Immersed Boundaries",* 1999, Journal of Computational Physics, v. 156, p. 209-240.

[28]. Marella, S, et.al*, "Sharp interface Cartesian grid method I: An easily implemented technique for 3D moving boundary computations"*, 2005, Journal of Computational Physics, v.210, p. 1-31.

[29]. Ge, L, *"Numerical simulation of flow in mechanical heart valves: grid resolution and the assumption of flow symmetry",* 2003, Journal of Biomechanical Engineering, v. 125, p. 709-18.

[30]. Ge, L, et.al. *"Flow in a mechanical bileaflet heart valve at laminar and near-peak systole flow rates: CFD simulations and experiments."* 2005, Journal of Biomechanical Engineering, v. 127, p. 782-97.

[31]. Wriggers. P, *"Nonlinear finite element methods",* 2008, Springer, Chapter 3, p. 82.

[32]. Vu-Quoc, L and Tan. X. G, *"Optimal solid shells for non-linear analyses of multilayer composites I Statics",* 2002, Computer Methods in Applied Mechanics and Engineering, v.192, p. 975-1016.

[33]. Vu-Quoc, L and Tan. X. G, "Optimal solid shells for non-linear analyses of multilayer composites. II. Dynamics", 2002, Computer Methods in Applied Mechanics and Engineering. v.192, p. 1017-1059.

[34]. Simo, J.C and Rifai, M.S, *"A class of mixed assumed strain method and the method of incompatible modes"*, 1990, International Journal for Numerical Methods in Engineering, v. 29, p. 1595-1638.

[35]. Dvorkin, E.N and Bathe, K.J, *"A continuum mechanics based four-node shell element for general non-linear analysis",* 1984, Engineering Computations, v. 1, p. 77–88.

[36]. Sun, W, "Biomechanical simulations of heart valve biomaterials", 2003, PhD Thesis, University of Pittsburgh.

[37]. Sun, W., et.al. *"Biaxial mechanical response of bioprosthetic heart valve biomaterials to high in-plane shear,"* 2003, Journal of Biomechanical Engineering, v. 125, p. 372-80.

[38]. Sun, W, and Sacks, M. S, *"Finite element implementation of a generalized Fungelastic constitutive model for planar soft tissues",* 2005, Biomechanics and Modeling in Mechanobiology, v. 4, p. 190-9.

[39]. Mirnajafi, A, et.al. *"The flexural rigidity of the aortic valve leaflet in the commissural region"* 2006, Journal of Biomechanical Engineering, v. 39, p. 2966-73.

[40]. Vigmostad, S. C and Udaykumar, H. S, "Algorithms for Fluid–Structure Interaction. Image-Based Computational Modeling of the Human Circulatory and Pulmonary systems by KB Chandran" Chapter 5, p. 191.

[41]. Marella, S, "Sharp interface Cartesian grid method I: An easily implemented technique for 3D moving boundary computations, Journal of Computational Physics", 2005, v. 210, p. 1-31.

[42]. Vigmostad, S.C, *"A sharp interface fluid-structure interaction model for bioprosthetic heart valve dynamics",* 2007, PhD Thesis, University of Iowa.

[43]. Michler, C. *"Efficient numerical methods for fluid-structure interaction",* 2005, PhD Thesis, Delft University of Technology: 161.

[44]. Causin, P, et.al. *"Added-mass effect in the design of partitioned algorithms for fluid-structure problems",* 2005, Computer Methods in Applied Mechanics and Engineering, v. 194, p. 4506-4527.

[45]. Lau, K.D, et.al, *"Fluid-structure interaction study of the edge-to-edge repair technique on the mitral valve",* 2011, Journal of Biomechanics, v. 44, p. 2409-2417.

[46]. Thubirkar, M, "The Aortic Valve", 1990, CRC Press, Boca Raton, Florida.

[47]. Mills, P, et.al, "The natural history of a non-stenotic bicuspid aortic valve", 1978, British Heart Journal, v.40, p. 951-57.

[48]. Wauchope, G, *"The clinical importance of variations in the number of cusps forming the aortic and pulmonary valves",* 1928, Quart Journal of Medicine, v. 21, p. 383-99.

[49] Braverman, A. C, et.al. *"The bicuspid aortic valve"*, 2005, Current Problems in Cardiology, v. 30, p. 470-522.

[50] Larson, E. W and Edwards, W. D, *"Risk factors for aortic dissection: a necropsy study of 161 cases"*, 1984, American journal of Cardiology, v. 53, p. 849-55.

[51] Ward, C, *"Clinical significance of the bicuspid aortic valve*", 2000, Heart, v. 83, p. 81-5.

[52] Wallby, L, et.al, *"T lymphocyte infiltration in non-rheumatic aortic stenosis: a comparative descriptive study between tricuspid and bicuspid aortic valves",* 2002, Heart, v. 88, p. 348-51.

[53] Eisenberg, L.M and Markwald, R.R, *"Molecular regulation of atrioventricular valvuloseptal morphogenesis",* 1995, Circulation Research, v. 77, p. 1-6.

[54] Fedak, P.W, et.al. *"Clinical and pathophysiological implications of a bicuspid aortic valve",* 2002, Circulation, v. 106, p. 900-4.

[55] Jermihov, P. L, et.al. *"Effect of Geometry on the Leaflet Stresses in Simulated Models of Congenital Bicuspid Aortic Valves",* 2011, Cardiovasc Eng Technol, v. 2, p. 48–56.

[56] Chandra, S. M., Rajamannan, N. M and Sucosky, P, *"Computational assessment of bicuspid aortic valve wall-shear stress: implications for calcific aortic valve disease"*, 2012, Biomechanics and Modeling in Mechanobiology, v. 11, p. 1085-1096.

[57] Weinberg, E. J., Mohammad, R and Mofrad, K, *"A multiscale computational comparison of the bicuspid and tricuspid aortic valves in relation to calcific aortic stenosis",* 2008, Journal of biomechanics, v. 41, p. 3482-3487.

[58] Robicsek, F, et.al. *"The congenitallybicuspidaortic valve: how does it function? Why does it fail?",* 2003, Presented at the Thirty-ninth Annual Meeting of The Society of Thoracic Surgeons, San Diego, CA, Jan 31–Feb 2.

[59] Nathan, D, P, et.al. *"IncreasedAscendingAorticWallStress in Patients With BicuspidAorticValves",* 2011, The Annals of Thoracic Surgery, v. 92, p. 1384–1389.

[60] Idelsohn, S. R, *"Fluid–structure interaction problems with strong added-mass effect",* 2009, International Journal for Numerical Methods in Engineering, v. 80, p. 1261–1294.

[61] Kuttler, U and Wall, A, *"Fixed-point fluid–structure interaction solvers with dynamic relaxation"*, 2008, Computational Mechanics, v. 43, p. 61-72.

[62] Aitken, C., *"Studies in practical mathematics II. The evaluation of the latent roots and latent vectors of a matrix"*, 1937, Royal Society of Edinburgh, v. 57, p. 269–304.

[63] Irons, B and Tuck, R., "*A version of the aitken accelerator for computer iteration"*, 1969, International Journal of Numerical Methods in Engineering, v. 1, p. 275–277.

[64] Schäfer, M., et.al. *"Efficient Numerical Simulation and Optimization of Fluid-Structure Interaction",* 2010, Fluid Structure Interaction II Lecture Notes in Computational Science and Engineering, , v. 73, p. 131-158.

[65] Baek, H and Karniadakis, G. E., *"A convergence study of a new partitioned fluid–structure interaction algorithm based on fictitious mass and damping*", 2012, Journal of Computational Physics, v. 231, , p. 629-652.

[66] Neumann, M, *"Robustness and efficiency aspects for computational fluid structure interaction",* 2006, Computational Science and High Performance Computing II, v. 91. Springer: Berlin, Heidelberg.

[67] FEAP–a finite element analysis program-Version 7.3 RL Taylor - University of California at Berkeley, 2000

[68] Conti, C. A, *"Biomechanical implications of the congenital bicuspid aortic valve: A finite element study of aortic root function from in vivo data",* 2010, The Journal of Thoracic and Cardiovascular Surgery, v. 140, p. 890-896.

[69] Peskin, C. S, *"The immersed boundary method",* 2002, Acta Numerica, v. 11, p. 479-517.

[70] Stockie, J. M. and Wetton, B. R., *"Analysis of stiffness in the immersed boundary method and implications for time-stepping schemes."* 1999, Journal of Computational Physics, v. 154, p. 41-64.

[71] Mousel, J., *"A Massively parallel adaptive sharp interface solver with application to mechanical heart valve simulation"*, 2012, Department of Mechanical Engineering, The University of Iowa.

[72] Higashidate, M, et.al. *"Regulation of the aortic valve opening: In vivo dynamic measurement of aortic valve orifice area"*, 1995, The Journal of Thoracic and Cardiovascular Surgery, v. 110, p. 496-503.